

International Journal of Design & Nature and Ecodynamics

Vol. 20, No. 9, September, 2025, pp. 1993-2010

Journal homepage: http://iieta.org/journals/ijdne

Magnetic Core/Shell Fe₃O₄@FA Nanocomposite for Visible Light Photocatalytic Degradation of Methyl Orange



Rusul Hussain Jaber^{1*}, Shahlaa Esmail Ebrahim¹, Fatehah Mohd Omar²

- ¹ Environmental Engineering Department, College of Engineering, University of Baghdad, Baghdad 10070, Iraq
- ² Environmental Engineering Department, Kampus Kejuruteraan, University Sains Malaysia, Nibong Tebal 14300, Malaysia

Corresponding Author Email: rusul.jaber2311@coeng.uobaghdad.edu.iq

Copyright: ©2025 The authors. This article is published by IIETA and is licensed under the CC BY 4.0 license (http://creativecommons.org/licenses/by/4.0/).

https://doi.org/10.18280/ijdne.200905

Received: 29 August 2025 Revised: 20 September 2025 Accepted: 24 September 2025 Available online: 30 September 2025

Available offine: 30 September 2

Keywords:

core/shell nanocomposite, Fe₃O₄, fly ash, methyl orange, photocatalysis, reusability, visible light, wastewater treatment

ABSTRACT

In this study, a magnetic nanocomposite based on iron oxide (Fe₃O₄) and modified fly ash (FA) was synthesized and evaluated as a visible light-driven photocatalyst for the removal of methyl orange (MO) dye from aqueous solutions. Two structural configurations, supported type Fe₃O₄/FA and core/shell Fe₃O₄@FA, were prepared using fly ash derived from the Al-Musayyib thermal power station in Iraq, with the latter synthesized through a thermal-assisted hydrothermal route. Comprehensive characterization (XRD, FESEM, FTIR, BET, VSM, and UV-Vis DRS) confirmed the successful formation of a stable heterojunction exhibiting enhanced crystallinity, surface area (45.6 m² g⁻¹), and superior magnetic and optical properties. The Fe₃O₄@FA composite displayed outstanding photocatalytic activity under visible light, achieving 92.7% degradation of MO within 90 min under optimal conditions (pH = 3, catalyst dose = 2 g L⁻¹, $H_2O_2 = 0.1$ M, MO = 10 ppm). In contrast, under initial conditions and without the addition of H₂O₂, the Fe₃O₄@FA composite achieved a degradation efficiency of 50.2%, indicating its inherent photocatalytic capability under visible light irradiation. Scavenger experiments identified hydroxyl radicals (*OH) as the predominant reactive species responsible for oxidation. The composite retained 77.2% of its initial activity after five successive cycles, demonstrating excellent magnetic recoverability and structural stability. This work underscores the potential of repurposing industrial fly ash into efficient, magnetically recoverable photocatalysts for sustainable wastewater treatment applications.

1. INTRODUCTION

Water is an essential resource for both life and industry, serving as a critical medium for numerous chemical processes. However, anthropogenic activities have significantly contributed to the pollution of surface water bodies, resulting in severe consequences for ecosystems and global water resources. The growing pressure on water availability presents a critical threat to environmental sustainability and human health [1]. Among various pollutants, dye-laden effluents from the textile industry pose a significant environmental challenge due to their high concentration and persistence of synthetic dyes. Azo dyes, such as methyl orange (MO), represent a major class of organic pollutants that are chemically and thermally stable, making them difficult to remove by conventional methods [2]. Traditional treatment techniques, including physical, chemical, and biological methods, are often ineffective in degrading these persistent compounds [3]. Consequently, there is a growing need to explore innovative and sustainable water treatment technologies. Semiconductor photocatalysts have emerged as promising candidates due to their potential in environmental remediation, water purification, and clean energy production [4]. Advanced oxidation processes (AOPs) have gained attention for their ability to generate hydroxyl radicals, which can oxidize and mineralize a wide range of organic pollutants [5]. Recent research has demonstrated that semiconductors can effectively photodegrade textile dyes in wastewater under light radiation. Various photocatalytic materials have been explored, including TiO₂, graphene, Ag-based compounds, metal oxide semiconductors, conducting polymers, and magnetic materials (ferrites and ferric-based composites) [6, 7]. However, several challenges remain, including degradation efficiency, limited stability, and the difficulty of regenerating and separating these catalysts, which hinders their application on an industrial scale [8]. This has motivated the search for low-cost, sustainable support materials to enhance the performance of photocatalysts [9].

One such material is fly ash (FA), an industrial byproduct generated from the combustion of oil in thermal power plants. After acid modification (e.g., HCl treatment), FA exhibits improved surface properties and reactivity, making it suitable for use as a photocatalyst support [10]. Various materials such as MnFe₂O₄, CuFe₂O₄, ZnFe₂O₄, and TiO₂ have been used as supported on FA or other substrates to enhance their photocatalytic performance [11-13]. Magnetic iron oxide nanoparticles (Fe₃O₄) have attracted attention due to their magnetic properties, ease of recovery, good adsorption

capacity, and ability to facilitate electron transfer between the photocatalyst and target molecules [14, 15]. However, Fe₃O₄ nanoparticles tend to aggregate due to their small size, leading to decreased surface area and reduced catalytic performance. To overcome this, Fe₃O₄ is often incorporated into support materials to improve dispersion and facilitate magnetic separation [16, 17].

Fly ash offers a chemically active surface rich in SiO₂ and Al₂O₃, which can stabilize Fe₃O₄ nanoparticles, enhance dispersion, and reduce magnetite dipole interactions [18, 19]. In this regard, fly ash can effectively act as a substitute for SiO₂ in traditional Fe₃O₄@SiO₂ core/shell systems. The FA shell provides a silica-like surface that is highly compatible with various surface functionalizations, while simultaneously offering economic and environmental advantages as a valorized industrial residue. However, the core/shell design also presents certain limitations, including the need for precise control over shell thickness and uniformity, potential diffusion barriers for reactant molecules, and longer synthesis times compared to simple supported photocatalysts. Nevertheless, these challenges are outweighed by the superior interfacial properties, recyclability, and photocatalytic efficiency achieved by the optimized Fe₃O₄@FA system. Compared with physically supported Fe₃O₄/FA composites, the core/shell configuration provides a more uniform distribution of Fe₃O₄ within the FA matrix, stronger interfacial coupling, and higher magnetic recyclability.

This integrated structure ensures more efficient charge transfer across the interface and minimizes the recombination of photogenerated carriers, leading to enhanced photocatalytic activity and long-term operational stability [20]. FA itself is a heterogeneous material primarily composed of unburned carbon and metal oxides such as Si, Fe, Ca, and Al. It is classified as Class F or Class C based on its oxide content, particularly SiO₂, Al₂O₃, Fe₂O₃, and SO₃ [21].

Many studies have investigated the use of FA to improve its economic value and reduce its environmental footprint, including applications in wastewater treatment, adsorbent production, zeolite synthesis, cement additives, and ceramic fillers [22, 23]. Beyond its structural and functional benefits, the incorporation of fly ash into photocatalysts represents a sustainable approach to reclaiming industrial residues into value-added materials for environmental remediation. Accordingly, this study aims to synthesize and evaluate a Fe₃O₄@FA core/shell nanocomposite as a visible light photocatalyst for the degradation of MO. We hypothesize that core/shell configuration will exhibit photocatalytic activity, charge separation efficiency, and operational stability compared to the supported type composite, owing to its enhanced interfacial contact and structural homogeneity. This research not only valorizes local fly ash waste into a high-performance photocatalytic material but also demonstrates a sustainable pathway for converting industrial residues into functional nanocomposites applicable in wastewater purification.

2. MATERIALS AND METHODS

2.1 Materials

Fly ash was collected from the Al-Musayyib oil-fired thermal power plant (Iraq) and stored in containers before use. Ferrous chloride tetrahydrate (FeCl₂·4H₂O, 98%), ferric

chloride hexahydrate (FeCl $_3$ ·6H $_2$ O $_3$, 98%) were obtained from Sigma-Aldrich (Europe) and Dae-Jung (Korea). Hydrochloric acid (HCl, 35–38 wt%), sodium hydroxide (NaOH, pellets), and hydrogen peroxide (H $_2$ O $_2$, 30 wt%) were supplied by Sigma-Aldrich (Germany). Methyl orange (MO) was purchased from Fisher Scientific (USA) and used as the model pollutant.

2.2 Modification of fly ash

Figure 1 illustrates the modification process of Iraqi fly ash (FA), which involves sequential washing and thermal treatment. FA is a major by-product of fossil-fuel-based power generation; at the Al-Musayyib oil-fired thermal power plant (Iraq), annual production is 5,000 t, creating storage and environmental burdens. According to chemical analysis, the untreated FA exhibits low SiO₂ (6.8 wt%) and a very high loss on ignition (LOI = 48 wt%) with moderate CaO (12.3 wt%), indicating substantial unburned carbon and entrained volatiles that limit surface reactivity and adsorption performance [24].

To improve its suitability for environmental applications, raw FA (10 g) was first calcined at 900°C for 3 h in air to reduce LOI by removing residual carbon and to dehydroxylate/stabilize the aluminosilicate framework, thereby enhancing surface reactivity and subsequent leaching efficiency. The calcined powder was then acid-activated in 3.5 M HCl (100 mL, room temperature, 3 h) under agitation. Afterward, the suspension was filtered, and the solid was rinsed with distilled water to a neutral pH. The modified FA was obtained by drying at 120°C for 12 h and storing in airtight containers before use [25]. This combined thermal acid protocol directly addresses the unusually high LOI of the Iraqi FA, yielding a cleaner, more reactive FA surface amenable to both supported (Fe₃O₄/FA) and core/shell (Fe₃O₄@FA) interfacial designs.

2.3 Synthesis of Fe₃O₄ MNPs

The co-precipitation approach was used to create Fe_3O_4 magnetic nanoparticles (MNPs). In this procedure, (0.006 mol, 1.622 g) of $FeCl_3 \cdot 6H_2O$ and (0.003 mol, 0.597 g) of $FeCl_2 \cdot 4H_2O$ were dissolved in 200 mL of deionized water at a molar ratio of 2:1. After 40 minutes of stirring at 60°C, 3 M of NaOH solution was added gradually (drop by drop) until the pH reached 11. An external magnet separated the produced Fe_3O_4 MNPs, and the water was drained. The Fe_3O_4 MNPs were washed three times with ethanol and deionized water to eliminate any remaining ions. The Fe_3O_4 nanoparticles were dried in an oven at $60^{\circ}C$ for 16 hours [26].

2.4 Synthesis of supported Fe₃O₄/FA nanocomposites

The Fe₃O₄/FA nanocomposites were synthesized by an insitu co-precipitation route [27]. Stoichiometric FeCl₃·6H₂O and FeCl₂·4H₂O (2:1 molar ratio) were dissolved in 50 mL of deionized water under magnetic stirring at 60°C. Modification FA was added to achieve a Fe₃O₄: FA weight ratio of 1:1 (w/w), and stirring continued for 40 min. Subsequently, 3 M NaOH was added dropwise while monitoring with a calibrated pH meter until pH = 11, inducing in-situ co-precipitation of Fe₃O₄ onto the FA surface and yielding a black suspension. The product was magnetically separated, washed with ethanol and deionized water until neutral pH, and dried at 60°C for 16 h, as illustrated in Figure 2.

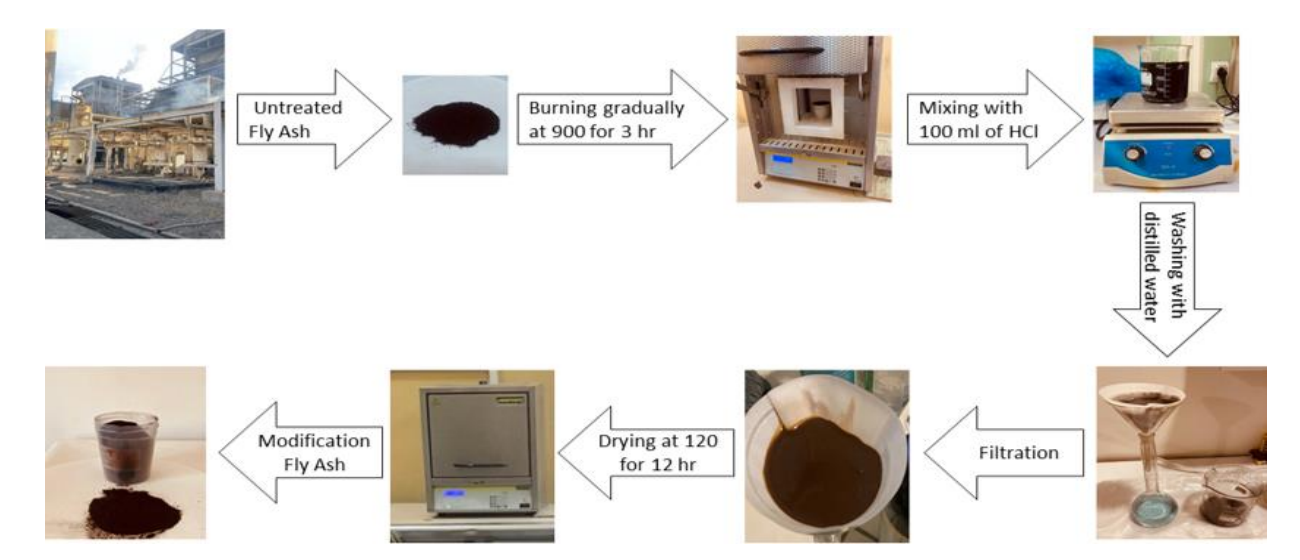


Figure 1. Modification of FA

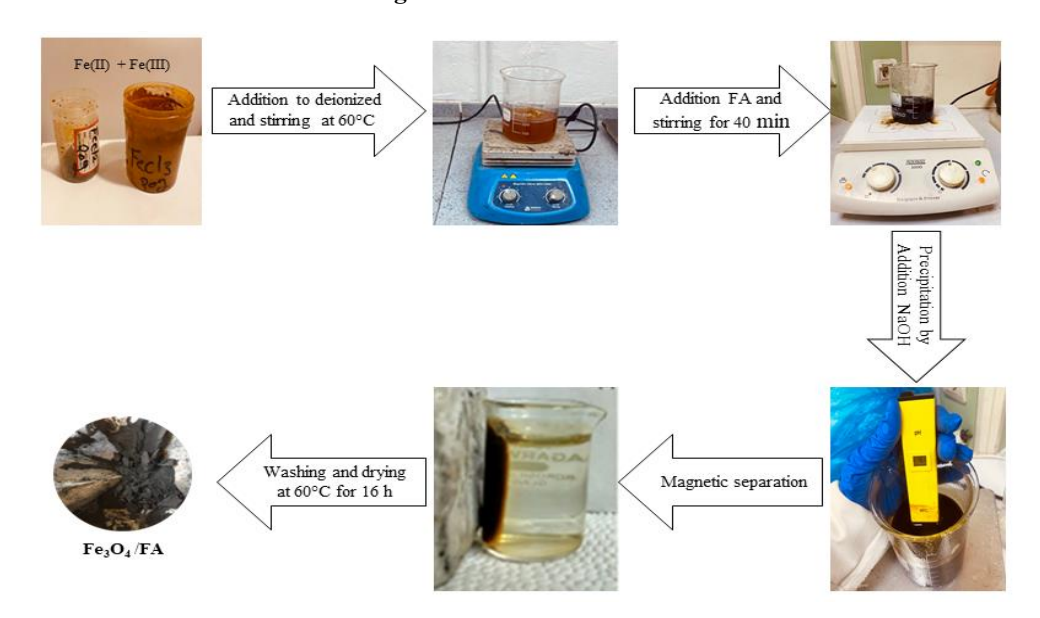


Figure 2. Fabrication of supported Fe₃O₄/FA photocatalyst

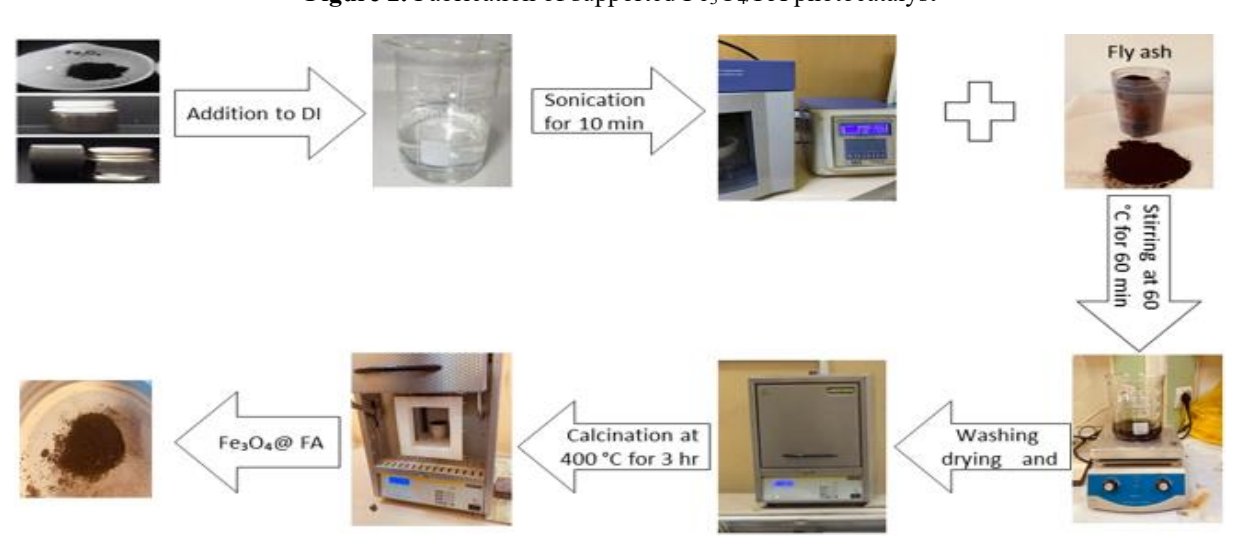


Figure 3. Fabrication of core/shell Fe₃O₄@FA photocatalyst

2.5 Synthesis of core/shell Fe₃O₄@FA nanocomposite

The Fe₃O₄@FA nanocomposite was prepared by a simple thermal-assisted mixing route, as illustrated in Figure 3. In a

typical procedure, Fe₃O₄ nanoparticles were ultrasonically dispersed in a small volume of deionized water for 10 min to obtain a uniform and stable suspension. Subsequently, an equal mass of modification FA powder (1:1 w/w) was

introduced into the Fe₃O₄ suspension, and the resulting mixture was continuously stirred at 60°C for 60 min to promote intimate interfacial contact and uniform coating of the FA layer around the Fe₃O₄ cores. The homogeneous slurry was then oven dried at 60°C for 16 h to remove residual moisture and achieve constant mass. The dried composite was subsequently calcined in air using a programmed heating profile: ramping from room temperature to 400°C at 8°C·min⁻¹, followed by a 130 min dwell at the same temperature. These controlled calcination steps enhanced crystallinity and reinforced the core/shell interfacial bonding while minimizing Fe₃O₄ oxidation. Finally, the calcined Fe₃O₄@FA nanocomposite was allowed to cool naturally to room temperature and stored in airtight containers for further characterization [20].

2.6 Characterization and equipment

The synthesized photocatalysts were characterized by X-ray diffraction (XRD), field emission scanning microscopy (FESEM), Fourier-transform infrared spectroscopy (FTIR), N₂ adsorption-desorption (BET/BJH), vibrating sample magnetometry (VSM), and UV-visible diffuse reflectance spectroscopy (UV-Vis DRS). XRD (AL-2700B, Cu K α , $\lambda = 0.15406$ nm) was performed at 40 kV and 30 mA over $10-80^{\circ}$ (20) with a 0.02° step and 2° min⁻¹ scan rate; peaks were indexed to ICDD standards and crystallite sizes estimated by the Scherrer equation. FESEM (ZEISS Ultra Plus) was used to assess morphology and dispersion. FTIR (Agilent) spectra were collected over 650-4000 cm⁻¹. Textural properties were obtained from N2 isotherms on a BET analyzer (BELSORP MINI II): samples were degassed at 150°C for 6 h under N2 and analyzed at 77 K to derive BET surface area, total pore volume, and BJH pore-size distribution (adsorption branch). Magnetic properties were measured at room temperature by VSM (VSM1100, Weistron) over -10,000 to +10,000 Oe. UV-Vis DRS (Hitachi U-3900H, 200-800 nm) data were converted via the Kubelka-Munk function, and apparent band gaps were determined from Tauc plots using the appropriate transition exponent (n).

2.7 Evaluation of photocatalytic degradation

The photocatalytic activity of MO was evaluated under visible light irradiation using two architectures: Fe₃O₄@FA and Fe₃O₄/FA. Tests were conducted in a batch reactor (1,000 mL Pyrex beaker; Figure 4). Illumination was provided by four 30 W BAOBAO BBI295 LED spotlights (white light; brightness comparable to xenon lamps) arranged symmetrically at the four corners of a 31.5 \times 20 cm base, each positioned 10 cm from the beaker wall [28].

The assembly was housed in a tightly sealed wooden enclosure with an exhaust fan; forced ventilation removed residual heat and vapors, maintaining the reaction near ambient temperature. According to the manufacturer, these LEDs emit within the visible range (400–780 nm) with negligible UV content. Based on the lamp geometry and optical efficiency, the irradiance at the solution surface was estimated to be approximately 20 mW cm⁻². Unless otherwise stated, runs were performed with 100 mL of a 20 mg L⁻¹ MO solution prepared in distilled water and a catalyst loading of 1 g L⁻¹. The suspension was maintained under gentle magnetic stirring to ensure homogeneous dispersion and uniform exposure of the catalyst to the light field. Before irradiation,

the mixture was stirred in the dark for 60 min to establish adsorption–desorption equilibrium [29], then irradiated for 90 min to initiate photodegradation. Aliquots (2 mL) were withdrawn every 15 min, promptly quenched by rapid magnetic separation, and filtered prior to UV–Vis analysis at 465 nm [30]. The degradation performance (DP) of the photocatalyst was calculated using Eq. (1) [30]:

$$DP(\%) = \frac{C_o - C_t}{C_o} \times 100\%$$
 (1)

where, C_0 is the initial MO (20 ppm), and C_t is the MO at a given time t during the photocatalysis process.



Figure 4. The batch photoreactor is utilized in the photocatalysis procedure

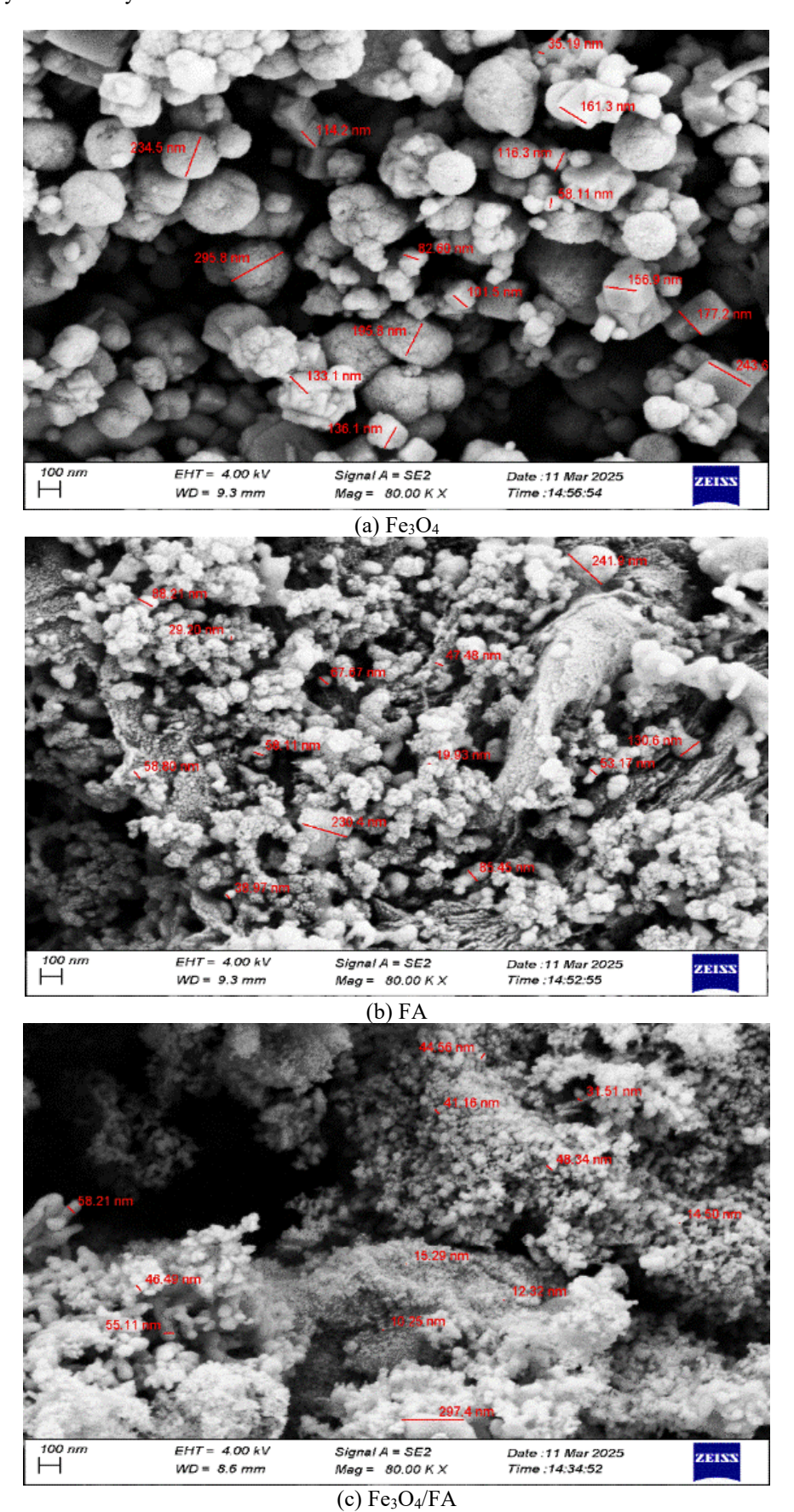
3. RESULTS AND DISCUSSION

3.1 Characteristics results

3.1.1 Morphological study

The morphological features of the synthesized photocatalysts were examined by FE-SEM. As shown in Figure 5(a), Fe₃O₄ nanoparticles display a quasi-spherical morphology with pronounced aggregation; magnetic agglomeration driven by strong interparticle interactions and high surface energy obscures particle boundaries, with individual sizes estimated at 80–120 nm [31].

As shown in Figure 5(b), raw fly ash exhibits highly irregular morphologies with rough, porous surfaces and a broad size distribution of approximately 300 nm to 2 μm, reflecting a heterogeneous aluminosilicate matrix with high adsorption potential [32]. As shown in Figure 5(c), the Fe₃O₄/FA composite shows Fe₃O₄ particles more uniformly distributed across the FA surface. The Fe₃O₄ particle size remains 90-120 nm, but aggregation is markedly reduced relative to bare Fe₃O₄, increasing interfacial contact with dve molecules. The FA scaffold serves as a support that limits severe agglomeration and provides anchoring sites, thereby enhancing the availability of photocatalytic sites [33]. Consistently, Fe₃O₄/FA demonstrated improved structural integration and favorable catalytic performance in degradation tests. Most notably, as shown in Figure 5(d), the core/shell Fe₃O₄@FA architecture reveals Fe₃O₄ cores of 100 nm encapsulated by a relatively uniform FA shell (30-50 nm thick). The shell mitigates core aggregation and improves dispersion in aqueous media while exposing additional active surface sites; it also couples the adsorptive capacity of FA with the magnetic photocatalytic core, which rationalizes the superior photocatalytic activity observed for this nanocomposite compared with both the bare and the supported counterparts [34].



1997

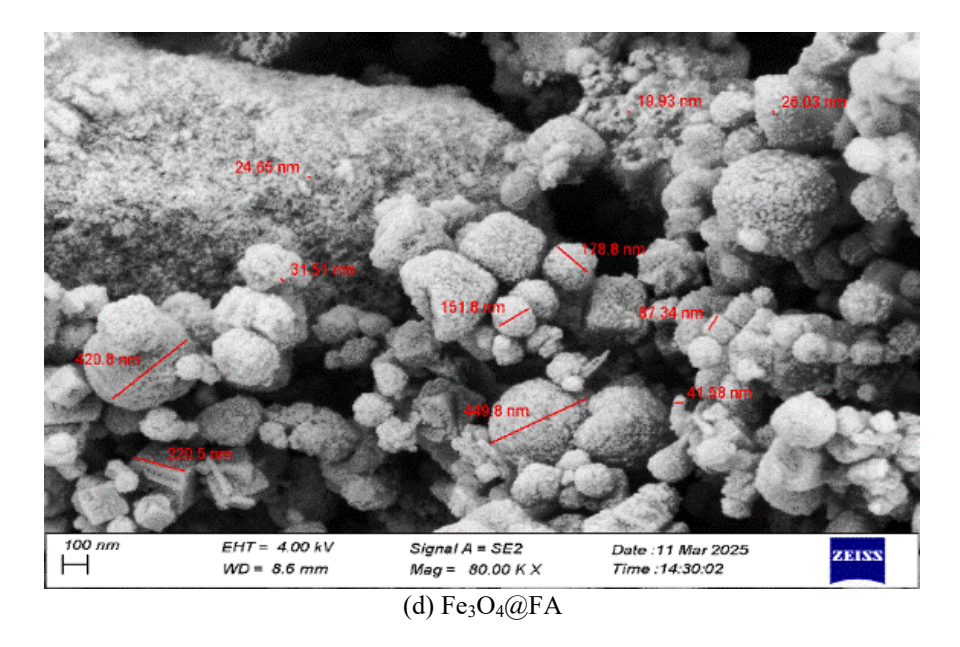
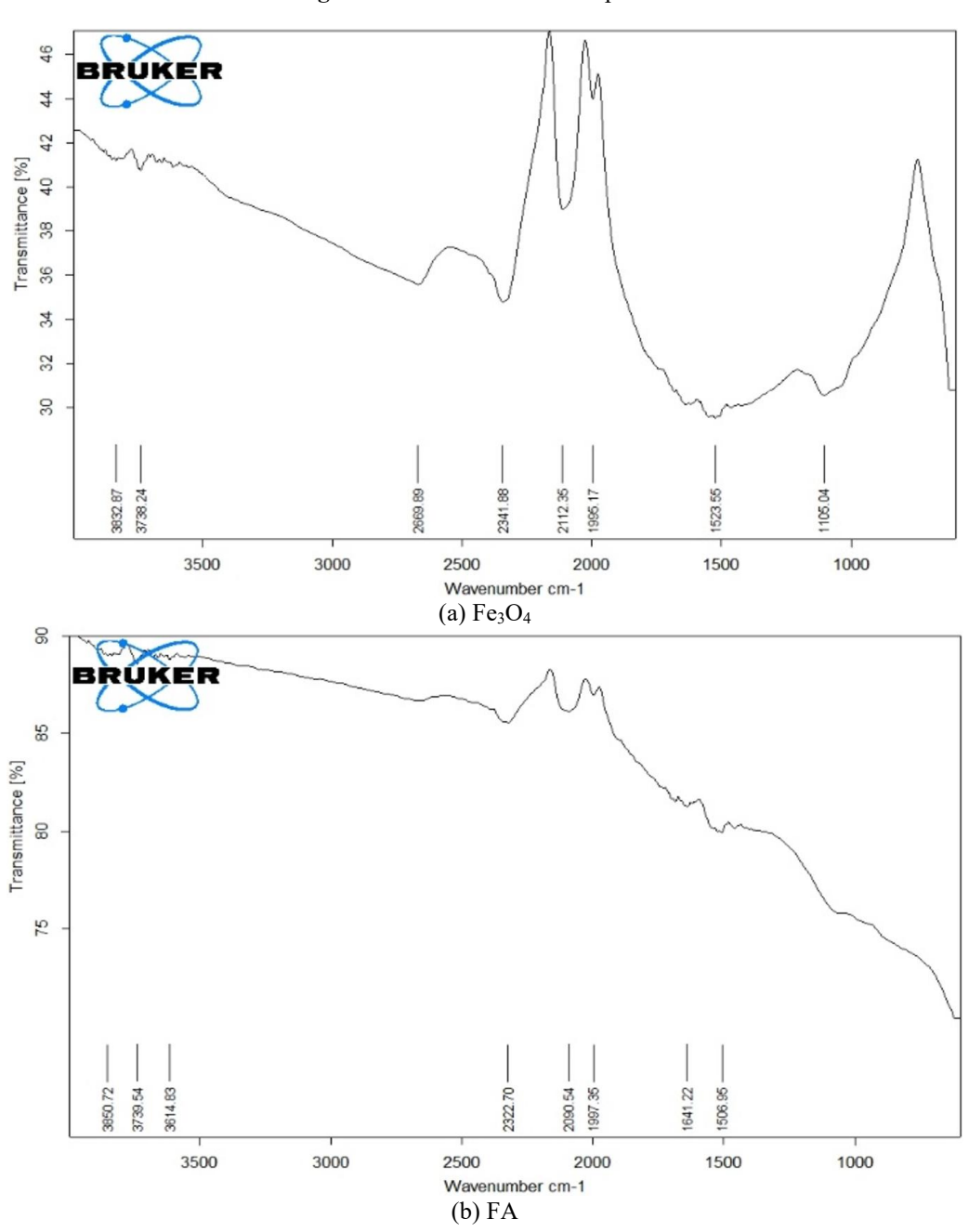


Figure 5. The FESEM for composites



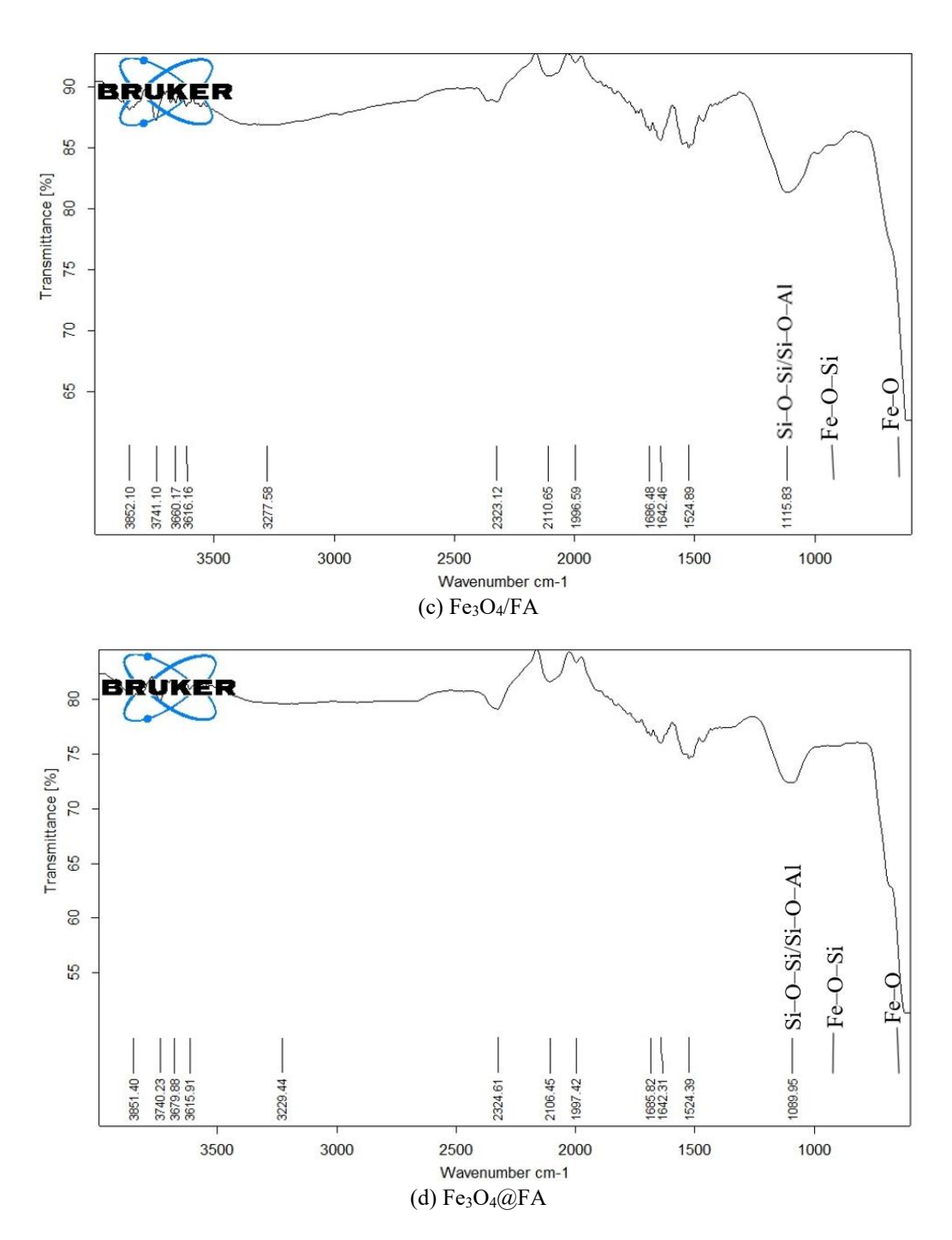


Figure 6. The FTIR for the composite

3.1.2 FTIR analysis

The FTIR spectra of Fe₃O₄, FA, Fe₃O₄/FA, and Fe₃O₄@FA composites, as shown in Figure 6(a–d), reveal distinct chemical interactions among the constituent phases. All samples exhibit a broad O–H stretching vibration near 3400 cm⁻¹, attributed to surface hydroxyl groups and adsorbed moisture. The intensity of this band is enhanced in both composites, particularly in Fe₃O₄@FA, owing to the presence of hydroxylated aluminosilicate phases derived from FA [35]. The bending mode of water molecules observed by 1630 cm⁻¹ further confirms the adsorption of moisture, a feature commonly reported for ferrite–silicate systems. As shown in Figure 6(b), the FA spectrum displays a strong band centered around 1005 cm⁻¹ corresponding to the asymmetric stretching of Si–O–Si/Si–O–Al bonds, which are typical of amorphous aluminosilicate frameworks.

A slight redshift to 960–980 cm⁻¹ in both the supported and

core/shell composites, as seen in Figures 6(c, d), indicates the formation of Fe–O–Si linkages, confirming interfacial chemical bonding between Fe₃O₄ and FA [36]. Additionally, a weaker band observed in the 780–820 cm⁻¹ region corresponds to the symmetric stretching of Si–O–Si groups, retained in all FA-containing samples [37].

Importantly, the Fe–O stretching vibration at 580–600 cm⁻¹ persists in all spectra, signifying the retention of the spinel ferrite structure of Fe₃O₄ even after hybridization. The combination of these features confirms the successful integration of FA into the Fe₃O₄ matrix while maintaining the structural integrity of magnetite. The Fe₃O₄@FA composite, as depicted in Figure 6(d), demonstrates clear structural evidence of interfacial Fe–O–Si bonding accompanied by pronounced surface hydroxylation. These features arise from the crystallinity improvement and controlled surface dissolution of Ca- and Fe-bearing phases during calcination at

400°C, which collectively promote the formation of Fe–O–Si linkages acting as efficient catalytic traps. Such interfacial structures enhance the adsorption and activation of dye molecules, thereby contributing to the superior photocatalytic performance observed for the composite [38, 39].

3.1.3 X-ray diffraction investigation

Figure 7 presents the XRD diffraction patterns of Fe₃O₄, FA, Fe₃O₄/FA, and Fe₃O₄@FA nanocomposites. The pure Fe₃O₄ sample shows distinct and sharp reflections at $2\theta = 30.2^{\circ}$, 35.5° , 43.2° , 53.4° , 57.3° , and 62.9° , corresponding

respectively to the (220), (311), (400), (422), (511), and (440) planes of the cubic spinel structure of magnetite (JCPDS No. 19-0629) [38]. The intense and well-defined (311) peak indicates high crystallinity and preferred crystal orientation. By applying Scherrer's equation to the most intense reflections, the average crystallite size of Fe₃O₄ was calculated to be approximately 28.5 nm, with a microstrain of about 7.8 \times 10⁻³ and a dislocation density near 5.8 \times 10⁻⁴ nm⁻². These results confirm that the prepared Fe₃O₄ nanoparticles possess a uniform spinel lattice with minimal structural defects.

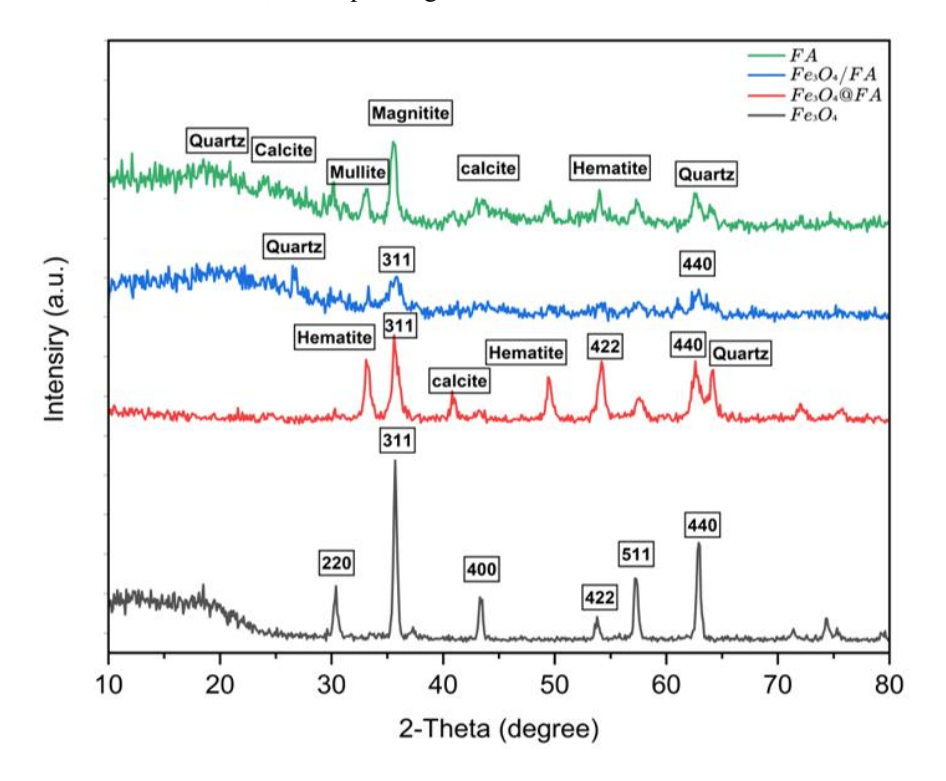


Figure 7. The XRD diffraction patterns of the synthesized photocatalysts

The XRD pattern of FA exhibits a broad amorphous hump extending between $2\theta = 20{\text -}35^\circ$, assigned to disordered aluminosilicate glassy phases typical of thermally generated FA [40]. Superimposed crystalline peaks at 26.6° (101) and 33.2° (112) correspond to quartz (SiO₂) and mullite (3Al₂O₃·2SiO₂), respectively, confirming that FA contains both amorphous and crystalline domains. This heterogeneous composition and fine structural disorder (estimated crystallite size = 15.5 nm) provide numerous active sites that can interact with Fe₃O₄ during composite formation.

For the Fe₃O₄/FA composite, the diffraction pattern retains all major Fe₃O₄ reflections together with the broad amorphous background of FA. However, the (311) peak becomes broader and less intense compared to pure Fe₃O₄, indicating the introduction of interfacial strain and partial lattice disorder resulting from Fe₃O₄ dispersion across the FA surface. The calculated crystallite size decreases to about 16.4 nm, suggesting that the FA matrix limits the crystal growth of Fe₃O₄ and promotes finer domain formation [41].

In contrast, the Fe₃O₄@FA nanocomposite displays all the characteristic spinel reflections of Fe₃O₄, particularly a moderately sharp peak at 35.5°, signifying that the magnetite phase remains intact after encapsulation. The crystallite size determined from multiple reflections averages 24.1 nm, while the microstrain and dislocation density decrease to 2.0×10^{-3}

nm⁻² and 5.4×10^{-3} , respectively. This slight increase in crystallite size relative to the supported sample, combined with the reduced strain, indicates that the FA shell acts as a structural buffer, minimizing lattice distortion and stabilizing the Fe₃O₄ crystalline core [42].

3.1.4 Surface properties

Figure 8 shows the N₂ adsorption—desorption isotherm of the Fe₃O₄@FA nanocomposite, which was analyzed to determine its surface texture and porosity. The isotherm exhibits a typical type IV profile with a distinct H₃ hysteresis loop, confirming the presence of a mesoporous structure. Prior to analysis, the sample (0.2003 g) was degassed at 120°C for 2 h under N₂ flow and analyzed at 77 K using a BELSORP MINI II surface area analyzer, ensuring complete removal of physisorbed moisture and gases.

According to the Brunauer–Emmett–Teller (BET) analysis, the nanocomposite possesses a specific surface area of 45.6 m² g⁻¹, a total pore volume of 0.141 cm³ g⁻¹, and an average pore diameter of 12.4 nm. These textural parameters clearly situate the material within the mesoporous domain (2–50 nm), which is highly favorable for adsorption and photocatalysis due to enhanced diffusion and improved accessibility of reactants to active surface sites [43, 44].

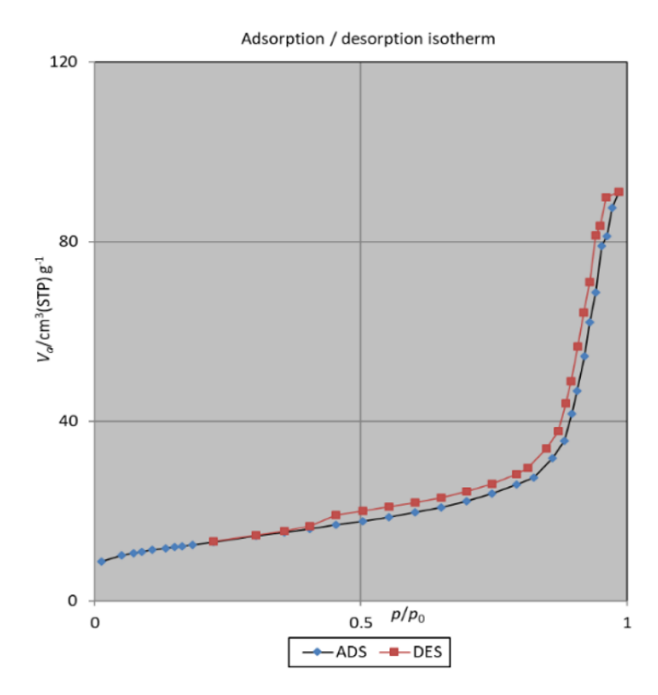


Figure 8. N₂ adsorption–desorption isotherm curves of Fe₃O₄@FA nanocomposite

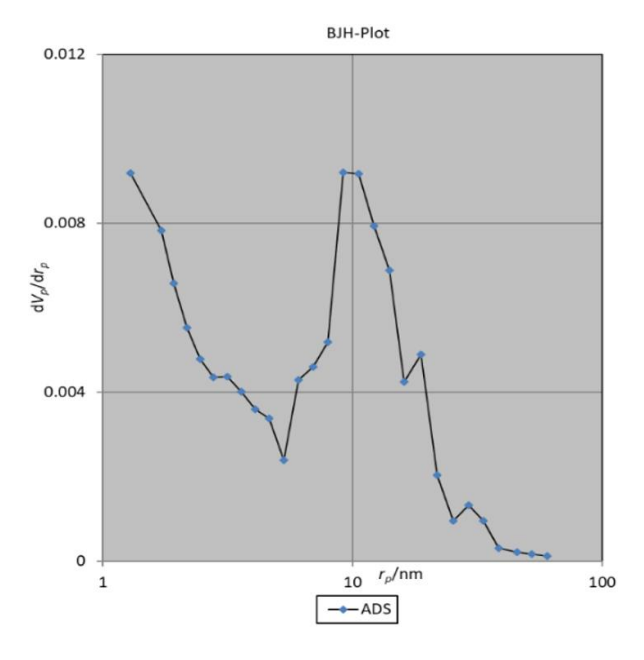


Figure 9. BJH-plot of Fe₃O₄@FA nanocomposite

The Barrett-Joyner-Halenda (BJH) pore-size distribution, shown in Figure 9, exhibits a unimodal peak centered at 9.21 nm, confirming a narrow and uniform pore distribution typical of FA-derived aluminosilicates. The H₃ hysteresis loop reflects slit like pores originating from the layered FA shell, which promotes efficient capillary condensation and reactive species diffusion. Compared with pure Fe₃O₄ nanoparticles, whose surface area typically ranges between 30 and 40 m² g⁻¹ [45], the observed increase in BET surface area for the Fe₃O₄@FA composite can be attributed to the incorporation of porous aluminosilicate components from fly ash. These amorphous phases introduce additional surface roughness, inhibit the magnetic aggregation of Fe₃O₄ nanoparticles, and promote the formation of interconnected pore channels [33]. Moreover, the enhanced surface area and well-defined pore network are strongly correlated with the improved photocatalytic performance of the Fe₃O₄@FA composite. A higher surface area facilitates efficient light harvesting and generates more active reaction sites, while mesoporous channels accelerate mass transport during dye adsorption and degradation. Similar enhancements in surface textural properties and catalytic efficiency have been reported for magnetically modified aluminosilicate materials, confirming that the synergistic combination of Fe_3O_4 and fly ash effectively promotes adsorption—photodegradation coupling [46].

3.1.5 The magnetic properties of photocatalysts

As shown in Figure 10, vibrating sample magnetometry (VSM) was employed to evaluate the magnetic response of Fe₃O₄, Fe₃O₄/FA, and Fe₃O₄@FA. The Fe₃O₄ nanoparticles exhibited a high saturation magnetization $(M_s) = 60$ emu g⁻¹, consistent with a well-crystallized spinel magnetite phase; however, superparamagnetism is more reliably inferred from the loop shape, namely the near-zero remanence and low coercivity that indicate soft magnetic behavior enabling rapid field on/field off response, rather than from M_s alone. In the Fe₃O₄/FA composite, M_s decreased to = 9.2 emu g⁻¹, which is to mass dilution by the non-magnetic attributed aluminosilicate matrix, increased interparticle spacing that weakens dipolar coupling, and interfacial "dead-layer" spin disorder at Fe₃O₄ and FA contacts [47]. In contrast, the Fe₃O₄@FA composite displayed $M_s = 37.3$ emu g⁻¹, markedly higher than the supported structure at the same Fe₃O₄ loading, because the encapsulation geometry forms a coherent magnetic core and a continuous FA shell that minimizes surface spin canting/oxidation and preserves interparticle exchange pathways through improved structural homogeneity [6]. The S-shaped hysteresis loop with narrow coercivity observed for Fe₃O₄@FA confirms soft-magnetic behavior and ensures efficient magnetic capture and redeployment of the catalyst during cyclic operation. Overall, the saturationmagnetization order Fe₃O₄ > Fe₃O₄@FA > Fe₃O₄/FA underscores the decisive role of architecture in balancing magnetic recoverability with interfacial stability, which is crucial for long-term photocatalytic reuse.

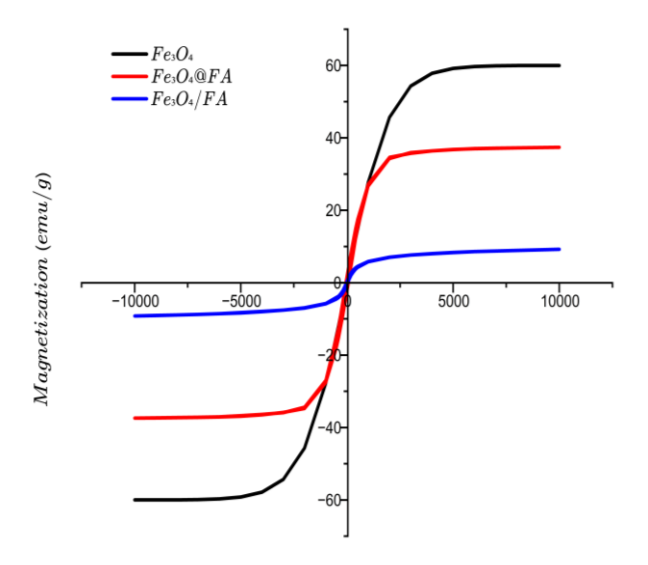


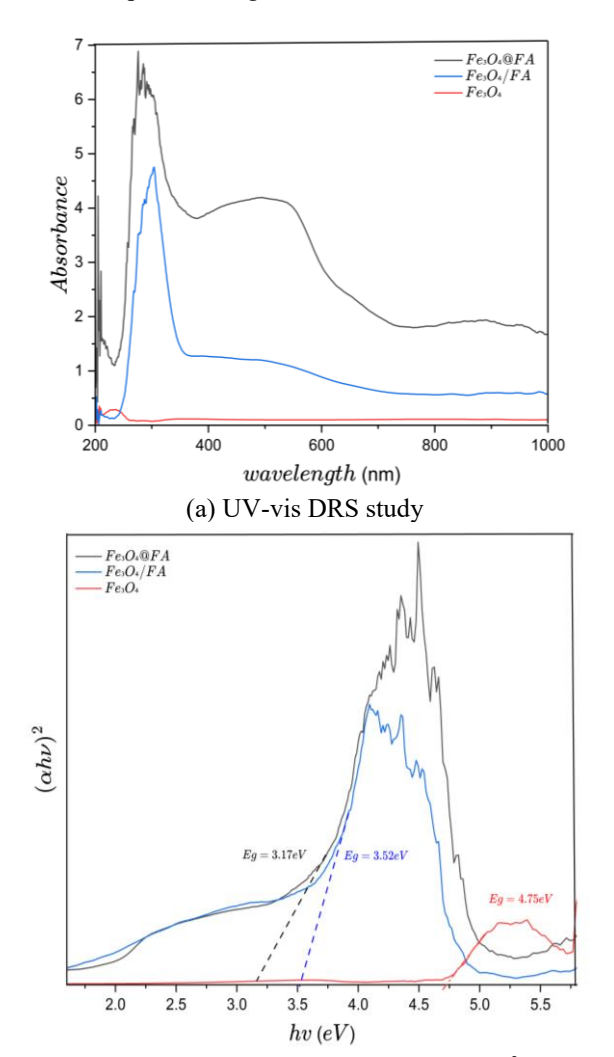
Figure 10. Synthetic photocatalysts' magnetic hysteresis curves

3.1.6 Optical characteristics of synthetic photocatalysts
Figure 11(a) shows the UV–Vis diffuse reflectance spectra
(DRS) of the synthesized photocatalysts, highlighting their

optical absorption behavior in the visible region. Among the examined materials, the Fe₃O₄@FA nanocomposite exhibited the most intense and extended absorption profile throughout the 400–800 nm range, significantly exceeding that of Fe₃O₄/FA and pure Fe₃O₄. This superior absorption is ascribed to enhanced interfacial charge transfer and electronic coupling between Fe₃O₄ and the amorphous aluminosilicate matrix of FA in the core/shell configuration, which facilitates light scattering suppression, homogeneous Fe₃O₄ dispersion within the FA shell, and improved charge mobility. Such synergistic effects collectively enhance visible light harvesting and photocatalytic activation [47, 48]. The optical band gap energy (Eg) of the samples was estimated from Tauc plots derived from the Kubelka–Munk function using Eq. (2):

$$\alpha h \upsilon = A(h \upsilon - Eg)^{n/2} \tag{2}$$

where α is the absorption coefficient, h is Planck's constant, v is the photon frequency, A is a proportionality constant, and n depends on the nature of the electronic transition (n = 2 for indirect transitions). The Eg value is determined from the intercept of the extrapolated linear portion of the $(\alpha h \nu)^2$ versus (h ν) curve [48, 49]. According to Figure 11(b), the calculated band gap energies were 3.17 eV for Fe₃O₄@FA, 3.52 eV for Fe₃O₄/FA, and 4.75 eV for pure Fe₃O₄, confirming a substantial red shift in the absorption edge of the composite relative to the pristine magnetite.



(b) optical bandgap utilizing Tauc graphs of $(\alpha h \nu)^2$ against hv

Figure 11. Photocatalysts' optical characteristics

The reduction of the band gap in the Fe₃O₄@FA composite implies that the composite structure enhances electron delocalization and interfacial energy level alignment, allowing photoexcitation of charge carriers under visible light irradiation. Notably, the pure Fe₃O₄ sample with its wider band gap of 4.75 eV absorbs predominantly in the ultraviolet region ($\lambda = 260$ nm), thereby exhibiting poor photocatalytic activity under visible light. In contrast, the narrowed band gap of the Fe₃O₄@FA composite facilitates electron—hole generation upon solar illumination, improving charge separation and minimizing recombination losses. Consequently, the optical data strongly corroborate the enhanced visible light-driven photocatalytic efficiency observed for the Fe₃O₄@FA nanocomposite compared to its supported and pristine counterparts.

3.2 Photocatalytic degradation

The degradation of MO under visible light irradiation without H₂O₂ was used to evaluate the intrinsic photocatalytic activity of the synthesized materials (Figure 12). Distinct differences were observed among the samples, demonstrating the influence of chemical composition and structural architecture on photocatalytic performance. FA exhibited the highest removal of MO during the dark adsorption stage, reaching 44% after 60 min and 52.7% after 90 min of visible light exposure. This behavior results from FA's complex surface composition rich in SiO₂ (54.4%), Al₂O₃ (14.96%), CaO (18.6%), and Fe₂O₃ (5.84%) its inherently porous texture that offers abundant hydroxyl and basic sites. These active sites facilitate dye adsorption and contribute to limited photoactivity under visible light, consistent with earlier reports on thermally activated fly ash [49, 50].

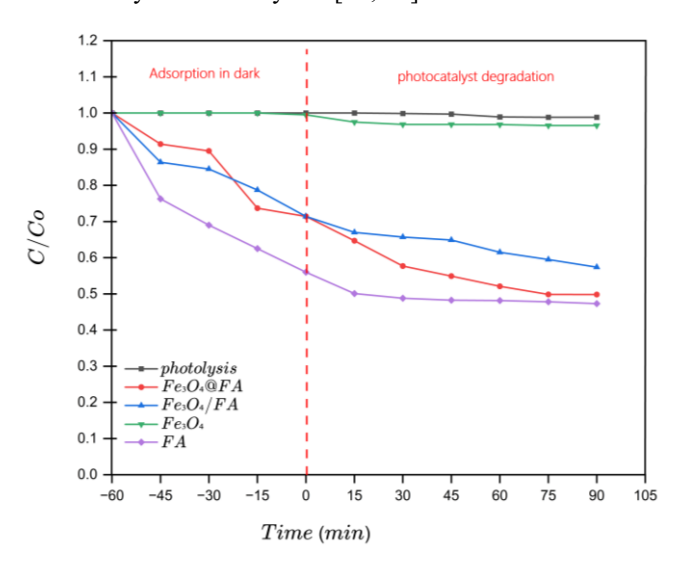


Figure 12. Photocatalytic degradation performance of MO using the photocatalysts at 1 g L⁻¹, without H₂O₂, at pH 7.5, and with an initial MO concentration of 20 ppm

After coupling FA with Fe₃O₄, the overall adsorption capacity decreased slightly because magnetic nanoparticles partly covered the open pores and reduced the optical reflectivity of the surface. However, the Fe₃O₄@FA composite still exhibited the highest photocatalytic degradation (50.2%), with an adsorption share of 28.6%. This improvement arises from the strong interfacial coupling between Fe₃O₄ and the aluminosilicate framework, which facilitates charge transfer,

broadens visible light utilization, and suppresses electron/hole recombination. The FA shell serves as a porous dielectric matrix that stabilizes Fe₃O₄ MNPs, enhances charge migration, and provides hydroxylated sites for the generation of reactive oxygen species (ROS) [50]. The Fe₃O₄/FA composite displayed moderate photocatalytic activity (42.6% MO removal), superior to pure Fe₃O₄ but lower than the core/shell material. Its relatively loose interface likely restricted charge-carrier transport and reduced the number of accessible reaction sites, confirming that the interfacial coherence achieved in the core/shell geometry is essential for efficient photocatalysis. As expected, pure Fe₃O₄ showed minimal degradation (3.45%) because of its wide band gap, limited surface area, and rapid charge carrier recombination under visible light [51]. In summary, although Fe₃O₄ loading slightly reduced the dye uptake ability of FA by masking part of its adsorption sites, the core/shell configuration markedly enhanced interfacial charge transfer and suppressed photocatalytic recombination; consequently, overall degradation improved despite the lower initial adsorption.

3.3 Impact of operational conditions

3.3.1 Impact of catalyst dosage

The photocatalytic activity of the $Fe_3O_4@FA$ composite was evaluated under visible light at varying catalyst dosages (0.5, 1, 2, and 3 g L^{-1}), with the results presented in Figure 13. All tests were conducted over a 90-minute irradiation period. The removal efficiency was found to be highly dependent on the catalyst dosage, reflecting the balance between surface active sites and light accessibility within the suspension.

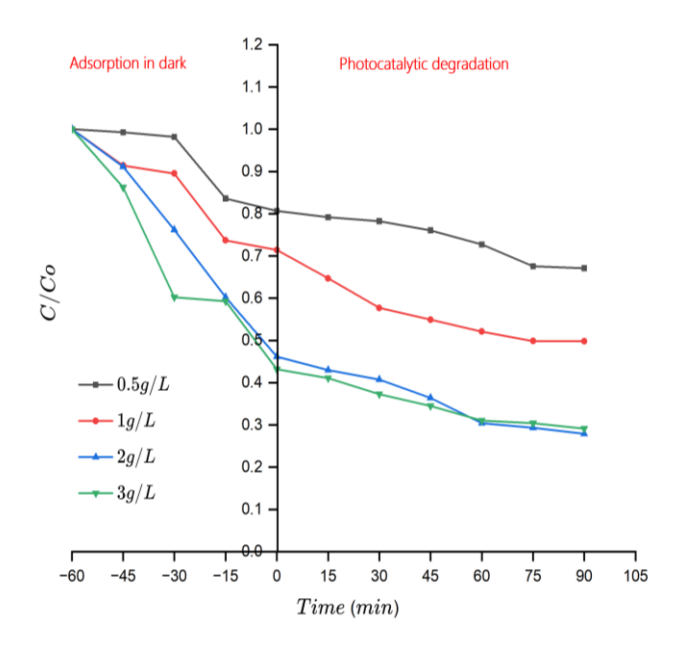


Figure 13. The influence of photocatalyst dosage on degradation activity at MO dye initial concentration = 20 ppm, without H_2O_2 and pH = 7.5

At the lowest dosage (0.5 g L⁻¹), the removal efficiency reached only 32.9%, likely due to the insufficient number of available active sites and limited light absorption. An increase to 1 g L⁻¹ significantly enhanced the degradation performance, achieving 50.2% removal, primarily due to the improved surface contact and photocatalytic activation. The highest efficiency was recorded at 2 g L⁻¹, with 72.1% removal after

90 minutes. This improvement can be attributed to the optimal dispersion of the catalyst and the increased number of reactive sites available for dye adsorption and photo-induced reactions.

Interestingly, further increasing the dosage to 3 g L^{-1} did not yield a substantial gain in performance, with a slight decrease to 70.85% observed. This marginal decline is most likely related to excessive catalyst loading, which can induce agglomeration and light scattering, thereby reducing the effective photon flux reaching the catalyst surface [52].

It is also worth noting that the catalyst dosage strongly influenced the initial adsorption behavior in the dark. Higher dosages resulted in more pronounced adsorption prior to irradiation, suggesting that the removal process benefits from a synergistic interplay between dye adsorption and subsequent photocatalytic degradation. This dual mechanism, particularly prominent at 2 g L^{-1} of Fe₃O₄@FA, appears to provide the most favorable conditions for efficient dye removal under visible light exposure.

3.3.2 The impact of MO concentration

Figure 14 shows that the photocatalytic activity of the $Fe_3O_4@FA$ nanocomposite was greatly influenced by the initial concentration of MO according to visible light exposure for 90 minutes in the absence of H_2O_2 . At a low dye concentration of 10 ppm, the nanocomposite achieved the highest degradation efficiency of 62.7%. However, as the concentration climbed to 20 and 30 ppm, the removal rate dropped to 50.2% and 47.9%, respectively.

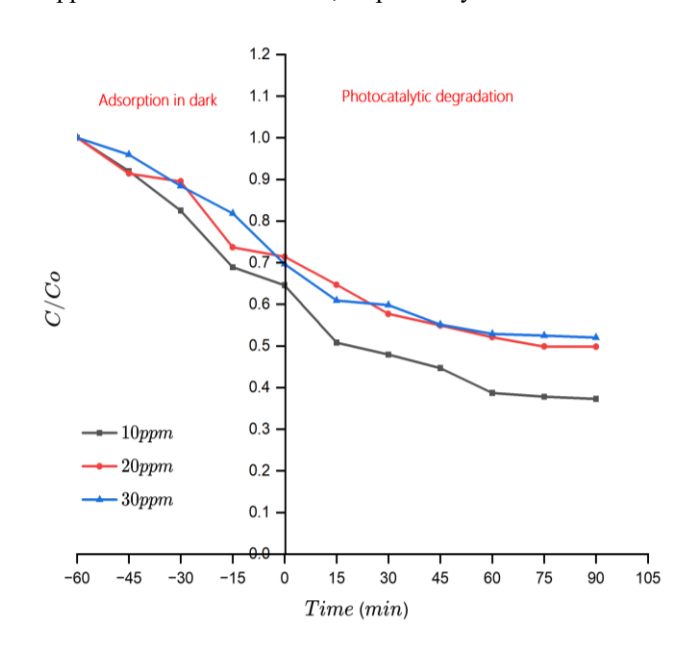


Figure 14. The impact of MO concentration on degradation efficiency under conditions of pH = 7.5, without H_2O_2 , and $dose = 1 \text{ g L}^{-1}$

This inverse correlation is well documented in heterogeneous photocatalysis and is mainly due to the saturation of the functional sites on the face of the photocatalyst at higher dye concentrations, as well as the increased optical density of the solution, which restricts light penetration and reduces photon absorption by the catalyst [53].

Moreover, the higher concentration of dye molecules may lead to the accumulation of intermediate products on the catalyst face, which can block functional sites and hinder the formation of reactive species, ultimately suppressing photocatalytic activity. At 10 ppm, the dye molecules are

sufficiently dispersed, allowing for more efficient adsorption on the composite surface and enhanced interaction with photogenerated electron/hole pairs. This condition promotes greater generation of ROS and consequently, higher degradation rates [54, 55]. These results underscore the importance of optimizing initial dye concentration to achieve effective photocatalytic degradation, particularly when working with visible light-responsive core/shell nanostructures.

3.3.3 The impact of pH

Figure 15 demonstrates that the initial pH of the solution significantly affects the photocatalytic degradation of MO utilizing the Fe₃O₄@FA composite under visible light irradiation. The degradation efficiency varied significantly over the measured pH range, with the catalyst dose at 1 g L⁻¹ and the initial dye concentration at 20 ppm. The highest removal efficiency, reaching 72%, was recorded at pH = 3, whereas moderate activity (50.2%) was observed at pH = 7.5, and a noticeable decline to 42.2% was seen at pH 11 after 90 minutes of irradiation. The increased photocatalytic activity in acidic media is most likely caused by a favorable electrostatic interaction between the photocatalyst's protonated surface and the anionic MO molecules. At lower pH, the composite's surface charge becomes more positive, improving adsorption, electron-hole separation, and producing reactive oxygen species such as hydroxyl radicals ('OH), leading to more efficient breakdown [56]. Electrostatic repulsion between the negatively charged surface of the catalyst and the anionic dye, which restricts surface interaction, is the cause of the activity drop at alkaline pH. Furthermore, the decreased efficiency under basic conditions may also be caused by the excess OHions in the solution scavenging 'OH radicals [57]. These findings underscore the importance of solution pH as a governing factor in photocatalytic systems, and support prior observations that acidic environments tend to favor improved photocatalytic activity for materials containing ferrite and fly ash constituents.

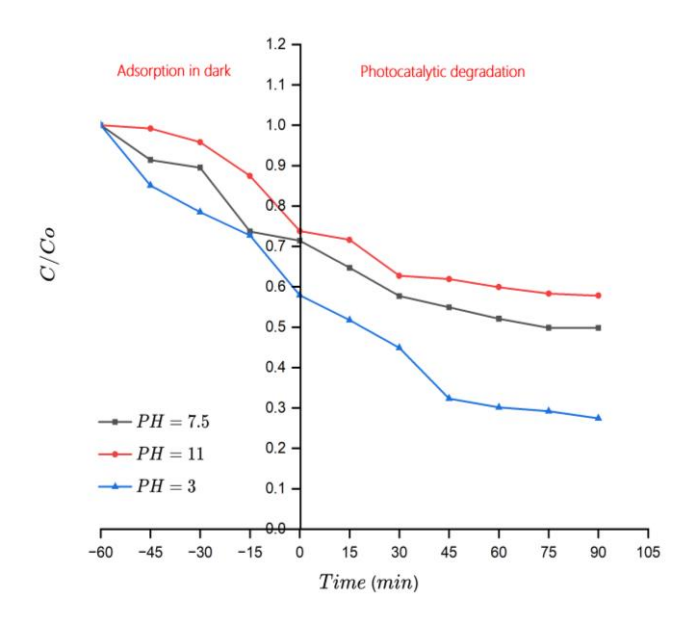


Figure 15. The impact of pH solution on the degradation of photocatalytic activity with operating conditions of dosage = 1 g L^{-1} , without H_2O_2 , and $C_0 = 20 \text{ ppm}$

3.3.4 The addition of H₂O₂

Under constant operational parameters (irradiation time: 90 minutes, catalyst dosage: 1 g L^{-1} , pH = 7, and MO initial concentration: 20 ppm), the addition of H_2O_2 was evaluated for its influence on the activity of photocatalytic $Fe_3O_4@FA$ composite. As illustrated in Figure 16, a baseline degradation efficiency of 50.2% was achieved without the presence of H_2O_2 , highlighting the inherent photocatalytic activity of the nanocomposite under visible light.

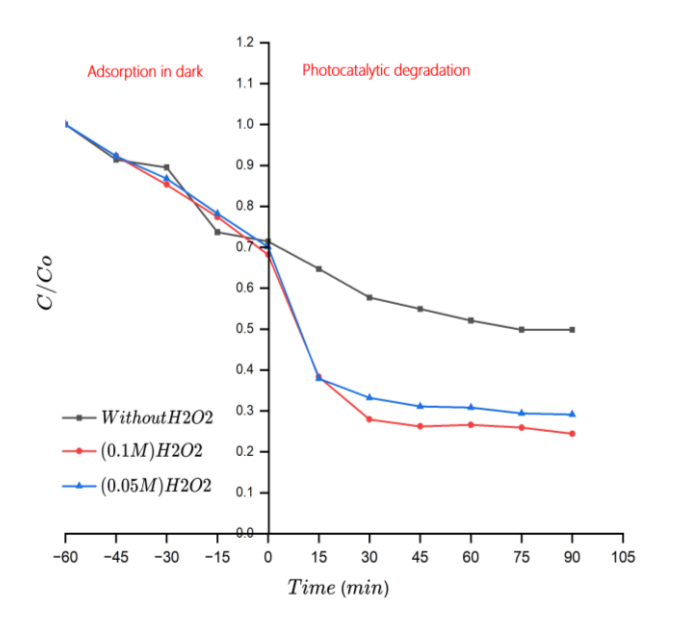


Figure 16. The impact of H_2O_2 concentration on MO efficiency of degradation under working conditions (pH = 7.5, $C_0 = 20$ ppm, and dosage = 1 g L⁻¹)

The introduction of 0.05 M $\rm H_2O_2$ significantly improved the degradation to 70.9%, while further increasing the concentration to 0.1 M resulted in a marginal enhancement, reaching 75.6%. The significant increase in efficiency underscores the importance of $\rm H_2O_2$ in generating ROS, specifically hydroxyl radicals ($\rm H_2O_2 \rightarrow 2'OH$), which accelerate the breakdown of dye molecules. The oxidant also helps to improve charge separation by scavenging electrons, which reduces recombination losses [58]. However, the marginal gain between 0.05 M and 0.1 M suggests the presence of an optimal concentration threshold, beyond which additional peroxide offers diminishing returns. Excessive $\rm H_2O_2$ may also participate in radical scavenging, effectively neutralizing ROS and limiting further degradation efficiency [59].

4. STABILITY AND REUSABILITY STUDIES

The long-term photocatalytic stability and reusability of the Fe₃O₄@FA nanocomposite were evaluated through five successive MO degradation cycles under fixed conditions (MO = 10 ppm, catalyst dosage = 2 g L⁻¹, H₂O₂ = 0.1 M, pH = 3, irradiation time = 90 min). As shown in Figure 17, the initial removal efficiency reached 92.7% in the first cycle and gradually decreased to 89.1%, 84.5%, 84.2%, and 77.2% in subsequent runs. This moderate attenuation indicates effective recyclability with limited deactivation across repeated use under oxidative conditions.

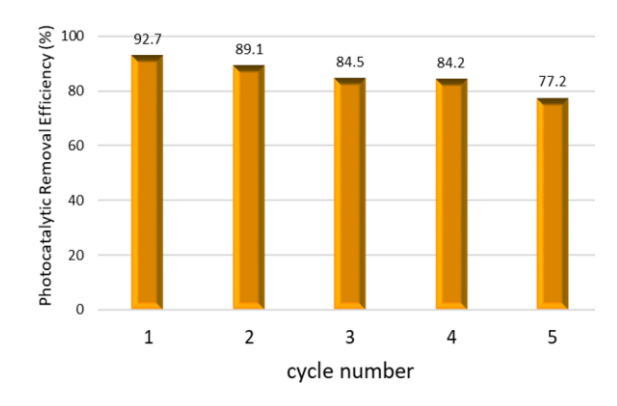
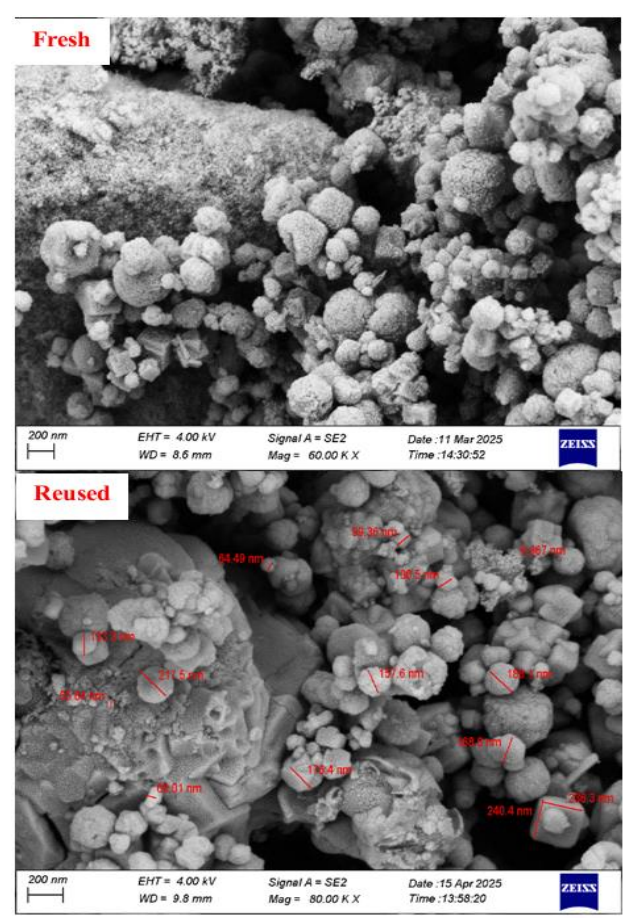
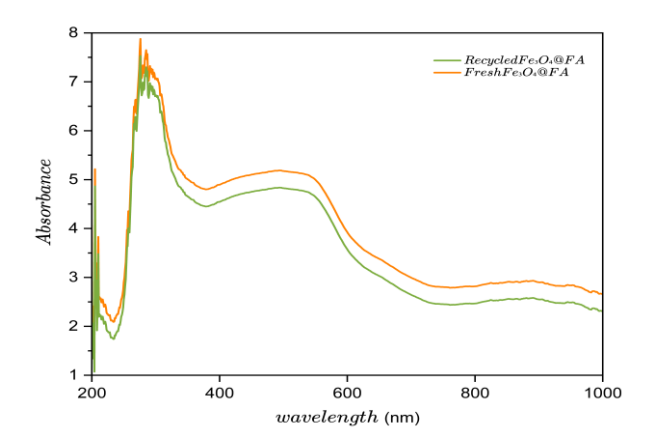


Figure 17. Synthesized photocatalysts were tested for stability and reusability throughout five running cycles with MO dye concentration = 10 ppm, $H_2O_2 = 0.1$ M, photocatalyst dosage = 2 g L^{-1} , pH = 3, and running time = 90 min

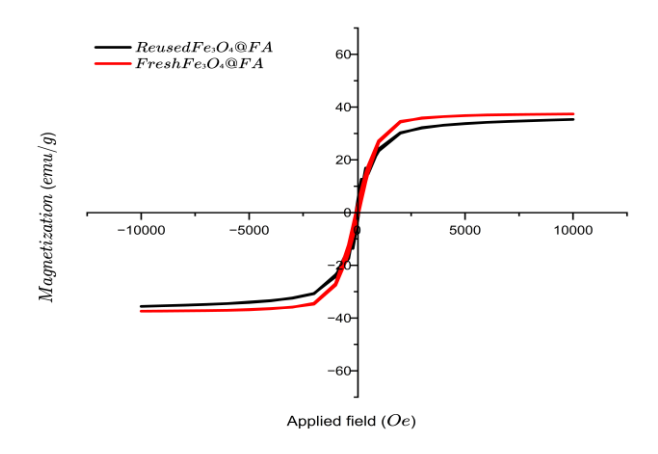
After each run, the powder was magnetically recovered, washed alternately with ethanol and distilled water (5 times) to remove adsorbed intermediates and residual oxidant, and dried at 60°C before reuse [30]. Structural and functional stability of the recycled catalyst. As shown in Figure 18(a-d), the catalysts maintained their structure and performance after five reuse cycles. FESEM (Figure 18(a)) reveals that the core/shell architecture and the characteristically rough surface are largely preserved, with only mild agglomeration. UV–Vis DRS (Figure 18(b)) exhibits nearly unchanged visible light absorbance, indicating that the light-harvesting capability remains intact. VSM and XRD (Figure 18(c, d)) further confirm retention of the soft-magnetic response and the spinel magnetite reflections, with only minor, non-significant variations that do not impair performance.



(a) FE-SEM



(b) UV-vis DRS curve



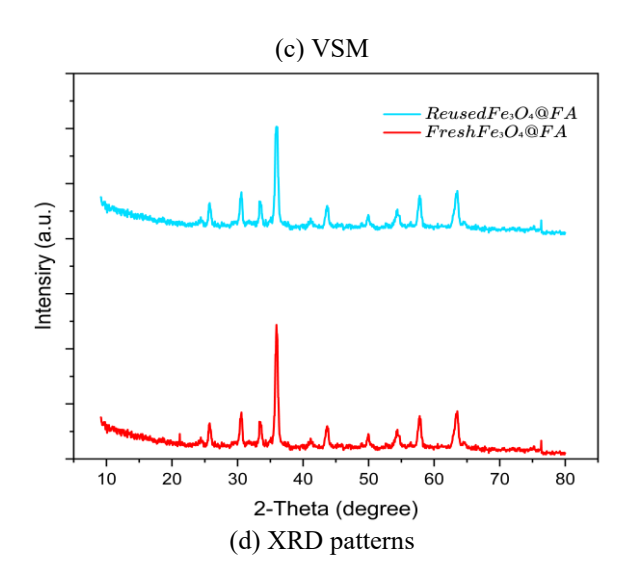


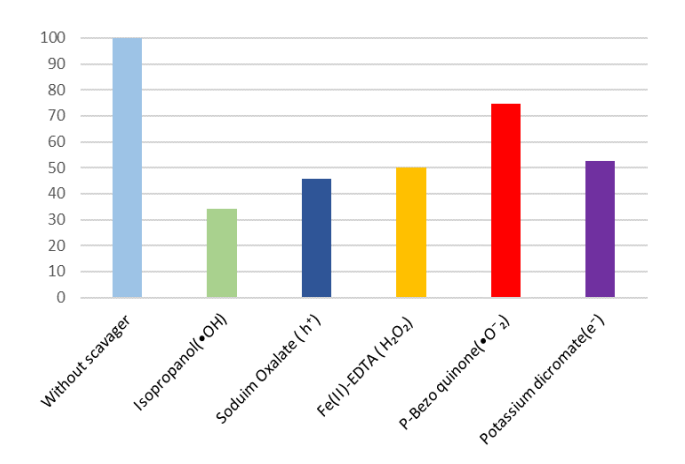
Figure 18. Characterization of fresh and reused Fe₃O₄@FA after the fifth cycle

The observed decline in activity is plausibly ascribed to surface fouling by partially oxidized by-products, transient masking/deactivation of active sites, and small material losses during washing/recovery. Notably, maintaining > 77% removal after five cycles under acidic, peroxide-assisted operation highlights the mechanical and interfacial robustness of the Fe₃O₄@FA design. The FA shell contributes to mechanical stability, mitigates irreversible aggregation, and

supports consistent magnetic separability, enabling practical reutilization in wastewater treatment [60].

5. SCAVENGER EXPERIMENTS AND PHOTOCATALYTIC MECHANISM

identify the dominant ROS governing the photodegradation of MO using the Fe₃O₄@FA nanocomposite, targeted scavenger experiments performed. Selective quenchers were introduced to intercept specific ROS: isopropanol for hydroxyl radicals (*OH), sodium oxalate for photogenerated holes (h+), Fe(II)-EDTA for hydrogen peroxide (H₂O₂), p-benzoquinone for superoxide radicals ('O₂-), and potassium dichromate for electrons (e-), as illustrated in Figure 19.



 $\begin{tabular}{ll} \textbf{Figure 19.} $Fe_3O_4@FA$ demonstrated photocatalytic removal efficiency against MO in the presence of various scavengers (MO dye initial concentration = 20 ppm, photocatalyst dosage = 1 g L^{-1}, running time = 90 min, and initial pH = 7.5) \\ \end{tabular}$

The most significant suppression of photocatalytic activity occurred in the presence of isopropanol, revealing 'OH as the predominant oxidative species in the degradation pathway. Noticeable but less pronounced declines were observed when using sodium oxalate and Fe(II)-EDTA, confirming that both h^+ and H_2O_2 participate meaningfully in the reaction mechanism. Conversely, the presence of potassium dichromate and p-benzoquinone caused minimal reduction, suggesting that e^- and ' O_2^- play minor roles in this system. Based on these outcomes, the descending order of ROS involvement can be summarized as follows:

$$^{\bullet}OH > h^{+} > H_{2}O_{2} > e^{-} > ^{\bullet}O_{2}^{-}$$

These findings are consistent with the band structure of Fe_3O_4 , which is considered the principal active phase within the composite. The band gap energy (Eg) of Fe_3O_4 was determined to be 4.75 eV, and the positions of the conduction band (CB) and valence band (VB) were calculated using Pearson's electronegativity method according to Eqs. (3)-(5) [61].

$$E_{VB} = X - Ee + 0.5Eg \tag{3}$$

$$E_{CB} = E_{VB} - Eg \tag{4}$$

where, Ee is the energy of free electrons on the hydrogen scale

(4.5 eV), and X is the absolute electronegativity of the composite, estimated via the geometric mean approach:

$$X(A_m B_n C_l) = \sqrt[m+n+l]{X_A^m X_B^n X_C^l}$$
 (5)

where, A, B, and C are the elements, and m, n, and l are the moles of these elements. Using these relations, the estimated positions of the CB and VB were -1.105 eV and +3.645 eV, respectively. This favorable band alignment allows the composite to operate efficiently under visible light, enabling a multi-step photocatalytic mechanism.

Upon irradiation with visible light, the composite absorbs photons and generates electron/hole pairs (Eq. (6)).

The excited electrons in the conduction band reduce dissolved oxygen to form superoxide radicals (Eq. (7)), which undergo protonation to yield hydroperoxyl radicals (Eq. (8)). These intermediates are subsequently reduced to form hydrogen peroxide (Eq. (9)), which, in turn, can be reduced by electrons to produce highly reactive hydroxyl radicals (Eq. (10)). Simultaneously, the photogenerated holes in the valence band oxidize water molecules or hydroxide ions to generate additional 'OH radicals (Eqs. (11) and (12)). These ROS synergistically attack MO molecules, resulting in complete mineralization into CO₂, H₂O, and other innocuous byproducts (Eq. (13)):

$$Fe_3O_4@FA + h\nu \rightarrow e^- + h^+ \tag{6}$$

$$e^- + O_2 \rightarrow {}^{\bullet}O_2^- \tag{7}$$

$${}^{\bullet}\mathrm{O}_{2}^{-} + \mathrm{H}^{+} \rightarrow \mathrm{HO}_{2}^{\bullet}$$
 (8)

$$HO_2 \cdot + e^- \rightarrow H_2O_2$$
 (9)

$$H_2O_2 + e^- \rightarrow {}^{\bullet}OH + OH^-$$
 (10)

$$h^+ + H_2O \rightarrow {}^{\bullet}OH + H^+$$
 (11)

$$h^+ + OH^- \rightarrow OH$$
 (12)

$${}^{\bullet}OH/h^{+}/H_{2}O_{2} + C_{14}H_{14}N_{3}SO_{3}Na \rightarrow CO_{2} + H_{2}O$$
 (13)

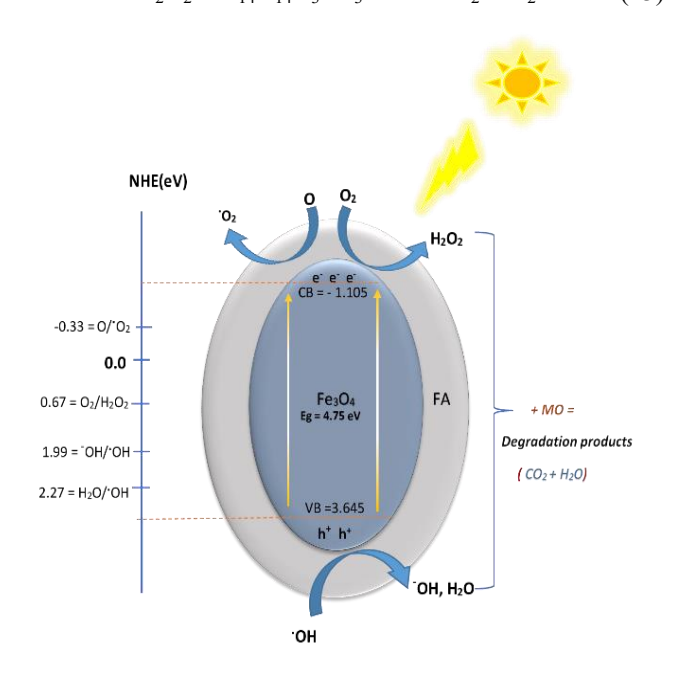


Figure 20. A possible pathway for MO photodegradation on the Fe₃O₄@FA surface

This mechanistic pathway aligns with the newly calculated CB and VB positions and demonstrates that the Fe₃O₄@FA composite exhibits sufficient redox potentials to promote the generation of both oxidative and reductive ROS (Figure 20).

The superior photocatalytic efficiency of Fe₃O₄@FA arises from the synergistic interplay between the active Fe₃O₄ phase and the porous fly ash support. The fly ash structure enhances surface adsorption and provides abundant surface hydroxyl groups that facilitate ROS formation. Meanwhile, Fe₃O₄ enables broad-spectrum light absorption and offers magnetic separability, allowing for easy recovery and reuse. This integration promotes effective charge separation, suppresses electron–hole recombination, and sustains ROS generation, thereby accelerating dye degradation under visible light irradiation.

6. CONCLUSIONS

The Fe₃O₄@FA magnetic nanocomposite was synthesized by a thermal-assisted mixing route and comprehensively evaluated by UV-Vis DRS, FESEM, VSM, FTIR, BET, and XRD, demonstrating a viable pathway to valorize industrial fly ash into a functional, magnetically separable photocatalyst. Owing to its core/shell architecture, the composite exhibited a narrowed optical band gap (3.17 eV versus 4.75 eV for pure Fe₃O₄), improved visible light harvesting, and more effective charge separation while mitigating nanoparticle aggregation collectively photocatalytic enhanced features that performance. Under optimized conditions (pH = 3, catalyst dose = 2 g L⁻¹, $H_2O_2 = 0.1$ M, MO = 10 ppm), the material achieved 92.7% removal within 90 min and retained 77.2% efficiency after five reuse cycles, confirming magnetic recoverability and structural durability.

Even without H₂O₂, the composite delivered 50.2% MO degradation under visible light, indicating intrinsic photocatalytic activity beyond dark stage adsorption. Mechanistically, the results are consistent with interfacial charge transfer at the Fe₃O₄ and FA junction and a dominant role for hydroxyl radicals (OH) in the oxidation pathway. Future investigations should focus on employing the Fe₃O₄@FA composite in continuous-flow photocatalytic reactors using real industrial effluents to validate its largescale applicability. Additionally, the incorporation of secondary magnetic oxides or co-catalysts could further enhance charge separation efficiency and overall degradation kinetics without compromising the adsorption properties provided by fly ash. Exploring hybridization with visible light active semiconductors (e.g., BiOCl, TiO2, or Ag2O) may also yield superior photoresponse and durability. Furthermore, extending its use toward the remediation of other environmental contaminants such as heavy metals, pesticides, fertilizers, and various organic dyes, as well as investigating its potential role in microbial immobilization and disinfection, would broaden its multifunctional application scope.

Ultimately, these proposed directions aim to bridge the gap between laboratory-scale synthesis and real-world environmental deployment, contributing to the advancement of sustainable photocatalytic technologies for wastewater purification and solid-waste utilization.

ACKNOWLEDGMENT

The authors gratefully acknowledge the Nanotechnology

and Advanced Materials Research Unit, College of Engineering, University of Kufa, for laboratory assistance and technical support.

REFERENCES

- [1] Luvhimbi, N., Tshitangano, T.G., Mabunda, J.T., Olaniyi, F.C., Edokpayi, J.N. (2022). Water quality assessment and evaluation of human health risk of drinking water from source to point of use at Thulamela municipality, Limpopo Province. Scientific Reports, 12: 6059. https://doi.org/10.1038/s41598-022-10092-4
- [2] Selvin, R., Hsu, H.L., Arul, N.S., Mathew, S. (2010). Comparison of photo-catalytic efficiency of various metal oxide photo-catalysts for the degradation of methyl orange. Science of Advanced Materials, 2(1): 58-63. https://doi.org/10.1166/sam.2010.1072
- [3] Chen, L., Meng, D., Wu, X., Wang, A., Wang, J., Wang, Y., Yu, M. (2016). In situ synthesis of V4+ and Ce3+ self-doped BiVO4/CeO2 heterostructured nanocomposites with high surface areas and enhanced visible-light photocatalytic activity. The Journal of Physical Chemistry C, 120(33): 18548-18559. https://doi.org/10.1021/acs.jpcc.6b04131
- [4] Saher, R., Hanif, M.A., Mansha, A., Javed, H.M.A., et al. (2021). Sunlight-driven photocatalytic degradation of rhodamine B dye by Ag/FeWO4/g-C3N4 composites. International Journal of Environmental Science and Technology, 18(4): 927-938. https://doi.org/10.1007/s13762-020-02888-6
- [5] Lopez-Lopez, C., Martín-Pascual, J., Martínez-Toledo, M.V., Muñío, M.M., Hontoria, E., Poyatos, J.M. (2015). Kinetic modelling of TOC removal by H2O2/UV, photo-Fenton and heterogeneous photocatalysis processes to treat dye-containing wastewater. International Journal of Environmental Science and Technology, 12(10): 3255-3262. https://doi.org/10.1007/s13762-015-0755-8
- [6] Harja, M., Buema, G., Lupu, N., Chiriac, H., Herea, D.D., Ciobanu, G. (2020). Fly ash coated with magnetic materials: Improved adsorbent for Cu (II) removal from wastewater. Materials, 14(1): 63. https://doi.org/10.3390/ma14010063
- [7] Mustafa, Y.A., Al-Jobouri, H.A., Jaid, K.M. (2014). Solar photocatalytic degradation of diuron in aqueous solution by TiO2. Journal of Engineering, 20(11): 80-90. https://doi.org/10.31026/j.eng.2014.11.06
- [8] Favier, L., Harja, M. (2021). TiO2/Fly Ash nanocomposite for photodegradation of organic pollutant. In Handbook of Nanomaterials and Nanocomposites for Energy and Environmental Applications, pp. 3051-3074. https://doi.org/10.1007/978-3-030-11155-7 11-2
- [9] Fayadh, A.H., Ebrahim, S.E., Kosaj, A.D. (2025). Efficient removal of methylene blue from wastewater using co-deposited NiFe3O4/MgO/Cr2O3 Nanocomposite under visible light irradiation. International Journal of Design & Nature and Ecodynamics, 20(6): 1203-1212. https://doi.org/10.18280/ijdne.200602
- [10] Visa, M., Isac, L., Duta, A. (2015). New fly ash TiO2 composite for the sustainable treatment of wastewater with complex pollutants load. Applied Surface Science, 339: 62-68.

- https://doi.org/10.1016/j.apsusc.2015.02.159
- [11] Fungaro, D.A., Yamaura, M., Carvalho, T.E.M. (2011). Adsorption of anionic dyes from aqueous solution on zeolite from fly ash-iron oxide magnetic nanocomposite. Journal of Atomic and Molecular Sciences, 2(4): 305-316. https://doi.org/10.4208/jams.032211.041211a
- [12] Huo, P., Yan, Y., Li, S., Li, H., Huang, W., Chen, S., Zhang, X. (2010). H2O2 modified surface of TiO2/fly-ash cenospheres and enhanced photocatalytic activity on methylene blue. Desalination, 263(1-3): 258-263. https://doi.org/10.1016/j.desal.2010.06.067
- [13] Qin, C., Li, H., Zhong, J., Li, J., Huang, S., Ma, L. (2021). Preparation of cypress leave-like Ag2WO4/BiVO4 heterojunctions with remarkably enhanced photocatalytic activity. Materials Letters, 283: 128793. https://doi.org/10.1016/j.matlet.2020.128793
- [14] Marroquin, J.B., Rhee, K.Y., Park, S.J. (2013). Chitosan nanocomposite films: Enhanced electrical conductivity, thermal stability, and mechanical properties. Carbohydrate Polymers, 92(2): 1783-1791. https://doi.org/10.1016/j.carbpol.2012.11.042
- [15] Li, G.Y., Jiang, Y.R., Huang, K.L., Ding, P., Chen, J. (2008). Preparation and properties of magnetic Fe3O4-chitosan nanoparticles. Journal of Alloys and Compounds, 466(1-2): 451-456. https://doi.org/10.1016/j.jallcom.2007.11.100
- [16] Chen, C.C., Chang, S.H., Shaya, J., Liu, F.Y., et al. (2022). Hydrothermal synthesis of BiOxBry/BiOmIn/GO composites with visible-light photocatalytic activity. Journal of the Taiwan Institute of Chemical Engineers, 133: 104272. https://doi.org/10.1016/j.jtice.2022.104272
- [17] Jabbar, Z.H., Ebrahim, S.E. (2022). Recent advances in nano-semiconductors photocatalysis for degrading organic contaminants and microbial disinfection in wastewater: A comprehensive review. Environmental Nanotechnology, Monitoring Management, 17: 100666. https://doi.org/10.1016/j.enmm.2022.100666
- [18] Su, C., Zhang, D., Pu, X., He, Z., Hu, X., Li, L., Hu, G. (2021).Magnetically separable NiFe2O4/Ag3VO4/Ag2VO2PO4 Z-scheme direct with enhanced visible-light heterostructure of Chemical Technology photoactivity. Journal 2976-2985. Biotechnology, 96(10): https://doi.org/10.1002/jctb.6855
- [19] Li, N., Fu, F., Lu, J., Ding, Z., Tang, B., Pang, J. (2017). Facile preparation of magnetic mesoporous MnFe2O4@ SiO2- CTAB composites for Cr (VI) adsorption and reduction. Environmental Pollution, 220: 1376-1385. https://doi.org/10.1016/j.envpol.2016.10.097
- [20] Saputro, S., Mahardiani, L., Masykuri, M., Yamtinah, S. (2022). Modification of coal fly ash waste by using coreshell method for Cu2+ adsorbent material. Journal of Physics: Conference Serie, 2190(1): 012002. https://doi.org/10.1088/1742-6596/2190/1/012002
- [21] Cao, J., Dong, X., Li, L., Dong, Y., Hampshire, S. (2014). Recycling of waste fly ash for production of porous mullite ceramic membrane supports with increased porosity. Journal of the European Ceramic Society, 34(13): 3181-3194. https://doi.org/10.1016/j.jeurceramsoc.2014.04.011
- [22] Yu, X., Zhang, G., Cao, H., An, X., et al. (2012). ZnO@ ZnS hollow dumbbells-graphene composites as high-performance photocatalysts and alcohol sensors. New

- Journal of Chemistry, 36(12): 2593-2598. https://doi.org/10.1039/C2NJ40770A
- [23] Azzaz, A.A., Jellali, S., Hamed, N.B.H., El Jery, A., Khezami, L., Assadi, A.A., Amrane, A. (2021). Photocatalytic treatment of wastewater containing simultaneous organic and inorganic pollution: Competition and operating parameters effects. Catalysts, 11(7): 855. https://doi.org/10.3390/catal11070855
- [24] Al Rammahi, R., Rasin, F., Al Aani, F. (2019). Treatment fly ash of Al Musayyib thermal power plant to be used as a pozzolanic material. Kufa Journal of Engineering, 10(3): 90-99. http://dx.doi.org/10.30572/2018/kje/100306
- [25] Gilja, V., Katančić, Z., Krehula, L.K., Mandić, V., Hrnjak-Murgić, Z. (2019). Efficiency of TiO2 catalyst supported by modified waste fly ash during photodegradation of RR45 dye. Science and Engineering of Composite Materials, 26(1): 292-300. https://doi.org/10.1515/secm-2019-0017
- [26] Ammar, S.H., Abdulnabi, W.A. (2020). Synthesis, characterization and environmental remediation applications of polyoxometalates-based magnetic zinc oxide nanocomposites (Fe3O4@ ZnO/PMOs). Environmental Nanotechnology, Monitoring Management, 13: 100289. https://doi.org/10.1016/j.enmm.2020.100289
- [27] Mushtaq, F., Zahid, M., Mansha, A., Bhatti, I.A., Mustafa, G., Nasir, S., Yaseen, M. (2020). MnFe2O4/coal fly ash nanocomposite: A novel sunlight-active magnetic photocatalyst for dye degradation. International Journal of Environmental Science and Technology, 17(10): 4233-4248. https://doi.org/10.1007/s13762-020-02777-y
- [28] Al Saady, S.H., Ebrahim, S.E. (2024). Efficient photocatalytic degradation of methylene blue using magnetic CoFe2O4@CuO@Ag3VO4 nanocomposite. International Journal of Design & Nature and Ecodynamics, 19(6): 1837-1846. https://doi.org/10.18280/ijdne.190601
- [29] Alkurdy, F.A.R., Ebrahim, S.E. (2020). Comparison between commercial and synthesized Fe3O4 nanoparticles for removal of heavy metal contaminants in wastewater. Association of Arab Universities Journal of Engineering Sciences, 27(1): 30-43. https://doi.org/10.33261/jaaru.2019.27.1.004
- [30] Danish, M., Muneer, M. (2021). Excellent visible-light-driven Ni-ZnS/g-C3N4 photocatalyst for enhanced pollutants degradation performance: Insight into the photocatalytic mechanism and adsorption isotherm. Applied Surface Science, 563: 150262. https://doi.org/10.1016/j.apsusc.2021.150262
- [31] Karvelas, E.G., Lampropoulos, N.K., Benos, L.T., Karakasidis, T., Sarris, I.E. (2021). On the magnetic aggregation of Fe3O4 nanoparticles. Computer Methods and Programs in Biomedicine, 198: 105778. https://doi.org/10.1016/j.cmpb.2020.105778
- [32] Eteba, A., Bassyouni, M., Saleh, M. (2023). Utilization of chemically modified coal fly ash as cost-effective adsorbent for removal of hazardous organic wastes. International Journal of Environmental Science and Technology, 20(7): 7589-7602. https://doi.org/10.1007/s13762-022-04457-5
- [33] Lu, C.G., Jiao, C.J., Zhang, X. C., Lin, W. C., Chen, X. F. (2025). Fly Ash-Supported photocatalysts: Synthesis,

- applications, and advances in modification technology. Crystals, 15(3): 223. https://doi.org/10.3390/cryst15030223
- [34] Cha, J.H., Choi, H.H., Jung, Y.G., Choi, S.C., An, G.S. (2020). Novel synthesis of core-shell structured Fe3O4@ SiO2 nanoparticles via sodium silicate. Ceramics International, 46(10): 14384-14390. https://doi.org/10.1016/j.ceramint.2020.02.233
- [35] Zhang, Z., Wang, H., Provis, J.L. (2012). Quantitative study of the reactivity of fly ash in geopolymerization by FTIR. Journal of Sustainable Cement-Based Materials, 1(4): 154-166. https://doi.org/10.1080/21650373.2012.752620
- [36] Mabu, D., Waleng, N.J., Munonde, T.S., Nqombolo, A., Nomngongo, P.N. (2025). Fe3O4/SiO2 nanocomposite derived from coal fly ash and acid mine drainage for the adsorptive removal of diclofenac in wastewater. Recycling, 10(3): 99. https://doi.org/10.3390/recycling10030099
- [37] Bakr, E.A., El-Nahass, M.N., Hamada, W.M., Fayed, T.A. (2021). Facile synthesis of superparamagnetic Fe3O4@ noble metal core-shell nanoparticles by thermal decomposition and hydrothermal methods: Comparative study and catalytic applications. RSC Advances, 11(2): 781-797. https://doi.org/10.1039/D0RA08230A
- [38] Ebrahim, S.E., Mohammed, S.Y. (2012). Removal of cadmium ions from simulated wastewater using rice husk biosorbent. Journal of Engineering, 18(07): 868-875. https://doi.org/10.31026/j.eng.2012.07.09
- [39] Alwash, A. (2016). Synthesis and characterization of CaMgO2 nanoparticles photocatalyst for the decolorization of orange G dye. Journal of Engineering, 22(11): 68-82. https://doi.org/10.31026/j.eng.2016.11.05
- [40] Izquierdo, M., Querol, X. (2012). Leaching behaviour of elements from coal combustion fly ash: An overview. International Journal of Coal Geology, 94: 54-66. https://doi.org/10.1016/j.coal.2011.10.006
- [41] Nadeem, N., Zahid, M., Rehan, Z.A., Hanif, M.A., Yaseen, M. (2022). Improved photocatalytic degradation of dye using coal fly ash-based zinc ferrite (CFA/ZnFe2O4) composite. International Journal of Environmental Science and Technology, 19(4): 3045-3060. https://doi.org/10.1007/s13762-021-03255-9
- [42] Oliveira-Filho, G.B., Atoche-Medrano, J.J., Aragón, F.F.H., Ochoa, J.M., Pacheco-Salazar, D.G., Da Silva, S.W., Coaquira, J.A.H. (2021). Core-shell Au/Fe3O4 nanocomposite synthesized by thermal decomposition method: Structural, optical, and magnetic properties. Applied Surface Science, 563: 150290. https://doi.org/10.1016/j.apsusc.2021.150290
- [43] Thommes, M., Kaneko, K., Neimark, A.V., Olivier, J.P., Rodriguez-Reinoso, F., Rouquerol, J., Sing, K.S. (2015). Physisorption of gases, with special reference to the evaluation of surface area and pore size distribution (IUPAC Technical Report). Pure and Applied Chemistry, 87(9-10): 1051-1069. https://doi.org/10.1515/pac-2014-1117
- [44] Nicola, R., Costişor, O., Muntean, S.G., Nistor, M.A., et al. (2020). Mesoporous magnetic nanocomposites: A promising adsorbent for the removal of dyes from aqueous solutions. Journal of Porous Materials, 27(2): 413-428. https://doi.org/10.1007/s10934-019-00821-y
- [45] Feng, L., Cao, M., Ma, X., Zhu, Y., Hu, C. (2012). Superparamagnetic high-surface-area Fe3O4

- nanoparticles as adsorbents for arsenic removal. Journal of Hazardous Materials, 217: 439-446. https://doi.org/10.1016/j.jhazmat.2012.03.073
- [46] Hong, T., Mao, J., Tao, F., Lan, M. (2017). Recyclable magnetic titania nanocomposite from ilmenite with enhanced photocatalytic activity. Molecules, 22(12): 2044. https://doi.org/10.3390/molecules22122044
- [47] Lai, C., Huang, F., Zeng, G., Huang, D., et al. (2019). Fabrication of novel magnetic MnFe2O4/bio-char composite and heterogeneous photo-Fenton degradation of tetracycline in near neutral pH. Chemosphere, 224: 910-921.
 - https://doi.org/10.1016/j.chemosphere.2019.02.193
- [48] Yang, K., Peng, H., Wen, Y., Li, N. (2010). Reexamination of characteristic FTIR spectrum of secondary layer in bilayer oleic acid-coated Fe3O4 nanoparticles. Applied Surface Science, 256(10): 3093-3097. https://doi.org/10.1016/j.apsusc.2009.11.079
- [49] Jing, H.P., Wang, C.C., Zhang, Y.W., Wang, P., Li, R. (2014). Photocatalytic degradation of methylene blue in ZIF-8. RSC Advances, 4(97): 54454-54462. https://doi.org/10.1039/C4RA08820D
- [50] Jasim, N.A., Ebrahim, S.E., Ammar, S.H. (2023). A comprehensive review on photocatalytic degradation of organic pollutants and microbial inactivation using Ag/AgVO3 with metal ferrites based on magnetic nanocomposites. Cogent Engineering, 10(1): 2228069. https://doi.org/10.1080/23311916.2023.2228069
- [51] Shaik, B., Kumari, A.M. (2025). A review on nanoparticles as a catalyst for biodiesel production. Results in Chemistry, 16: 102426. https://doi.org/10.1016/j.rechem.2025.102426
- [52] Jabbar, Z.H., Ebrahim, S.E. (2021). Highly efficient visible-light-driven photocatalytic degradation of organic pollutants by using magnetically separable supported heterogeneous nanocomposites (SiO2/Fe3O4/Ag2WO4). Environmental Nanotechnology, Monitoring Management, 16: 100554. https://doi.org/10.1016/j.enmm.2021.100554
- [53] Sreedharan, A., Ong, S.T. (2020). Combination of Plackett Burman and response surface methodology experimental design to optimize malachite green dye removal from aqueous environment. Chemical Data Collections, 25: 100317. https://doi.org/10.1016/j.cdc.2019.100317
- [54] Zimmer, A., Bergmann, C.P. (2007). Fly ash of mineral coal as ceramic tiles raw material. Waste Management, 27(1): 59-68. https://doi.org/10.1016/j.wasman.2006.01.009
- [55] Rauf, M.A., Ashraf, S.S. (2009). Fundamental principles and application of heterogeneous photocatalytic degradation of dyes in solution. Chemical Engineering Journal, 151(1-3): 10-18. https://doi.org/10.1016/j.cej.2009.02.026
- [56] Nguyen, T.D., Vu, X.M., Kouznetsova, T.F., Pham, T.L., et al. (2025). Advanced Mn3O4/Fe3O4-carbon molecular sieve composite: A robust catalyst for heterogeneous photo-fenton oxidation of organic dyes. Journal of Porous Materials, 32: 821-841. https://doi.org/10.1007/s10934-024-01741-2
- [57] Adday, R., Flayeh, H. (2025). Removal of methylene blue from wastewater using al haji plant as a low-cost, eco-friendly adsorbent. Al-Khwarizmi Engineering Journal, 21(2): 23-41.

- https://doi.org/10.22153/kej.2025.02.002
- [58] Neyens, E., Baeyens, J. (2003). A review of classic Fenton's peroxidation as an advanced oxidation technique. Journal of Hazardous Materials, 98(1-3): 33-50. https://doi.org/10.1016/S0304-3894(02)00282-0
- [59] Sahar, S., Zeb, A., Liu, Y., Ullah, N., Xu, A. (2017). Enhanced Fenton, photo-Fenton and peroxidase-like activity and stability over Fe3O4/g-C3N4 nanocomposites. Chinese Journal of Catalysis, 38(12): 2110-2119. https://doi.org/10.1016/S1872-2067(17)62957-7
- [60] Chatterjee, D., Ruj, B., Mahata, A. (2001). Adsorption

- and photocatalysis of colour removal from waste water using flyash and sunlight. Catalysis Communications, 2(3-4): 113-117. https://doi.org/10.1016/S1566-7367(01)00017-6
- [61] Singh, P., Raizada, P., Sudhaik, A., Shandilya, P., Thakur, P., Agarwal, S., Gupta, V.K. (2019). Enhanced photocatalytic activity and stability of AgBr/BiOBr/graphene heterojunction for phenol degradation under visible light. Journal of Saudi Chemical Society, 23(5): 586-599. https://doi.org/10.1016/j.jscs.2018.10.005